Chem Soc Rev

Synthesis of Metallic High-Entropy Alloy Nanoparticles

Journal:	*Chemical Society Reviews*
Manuscript ID	CS-REV-11-2023-000954.R1
Article Type:	Review Article
Date Submitted by the Author:	11-Feb-2024
Complete List of Authors:	Sun, Xiuyun; Dezhou University, College of Energy and Mechanical Engineering Sun, Yugang; Temple University, Department of Chemistry

Synthesis of Metallic High-Entropy Alloy Nanoparticles

Xiuyun Sun[1] and Yugang Sun[2,*]

[1] College of Energy and Mechanical Engineering, Dezhou University, Dezhou, Shandong, 253023, P.R.China

[2] Department of Chemistry, Temple University, 1901 North 13th Street, Philadelphia, Pennsylvania, 19122, USA

*E-mail: ygsun@temple.edu

Abstract

The theoretically infinite compositional space of high-entropy alloys (HEA) and their novel properties and applications have attracted much attention from a broader research community. The successful synthesis of high-quality single-phase HEA nanoparticles represents a crucial step to fully unlock the potential of this new class of materials in driving innovations. This review analyzes the many methods reported in the literature to identify their commonalities and dissimilarities, which allows categorizing these methods into five general strategies. Physical minimization of HEA metals into HEA nanoparticles through cryo-milling represents the typical top-down strategy. The counter bottom-up strategy requires the simultaneous generation and precipitation of metal atoms of different elements on growing nanoparticles. Depending on the metal atom generation process there are four synthesis strategies: vaporization of metals, burst reduction of metal precursors, thermal shock-induced reduction of metal precursors, and solvothermal reduction of metal precursors. The comparisons of the methods in each strategy and discussions provide insights and guidance to achieve the robust synthesis of HEA nanoparticles.

1. Introduction

Metal alloys are formed from homogeneous mixing of multiple elements in a crystalline solid-solution phase. According to the metallurgic phase diagrams, metal alloys are based on one or two principal elements, with some minor elements added to adjust their microstructures and properties. Alloys with multiple principal elements, or so-called high-entropy alloys (HEA), were first fabricated by Professor Chang's group[1] (Oxford University, UK) and Professor Yeh's group[2] (National Tsing Hua University, Taiwan) in 2004. Alloys composed of five or more elements with an atomic percentage of each element in the range of 5%-35% are described as high-entropy alloys (HEAs). The homogeneous mixing of constituent metal atoms increases the configuration entropy of the alloys, favoring their thermodynamic stability. The molar mixing entropy (ΔS_{mix}) for an ideal mixture containing a number of n elements is calculated by $\Delta S_{\mathrm{mix}} = -(\sum_{i=1}^{n} x_i \ln x_i) \times R$, in which x_i represents the mole fraction of element i and R is the molar gas constant (8.314 J·mol·K^{-1}). For instance, a HEA containing five elements at an equimolar ratio exhibits a system molar mixing entropy of 1.61R. In contrast, an alloy of two elements with equal amounts shows a system molar mixing entropy of only 0.69R.

From a thermodynamic point of view ($\Delta G_{\mathrm{mix}} = \Delta H_{\mathrm{mix}} - T \cdot \Delta S_{\mathrm{mix}}$), a higher mixing entropy in a HEA is beneficial for lowering the system's Gibbs energy. The mixing entropy of a HEA increases with the number of constituent elements and can act as a driving force for homogeneously mixing the metal atoms of different elements, particularly at high temperatures. On the other hand, the formation enthalpy (ΔH_{ij}) of metallic bonds between different elements varies widely depending on the characteristics (e.g., atom size and electron configuration) of the constituent elements,[3] which competes with the mixing entropy to determine the alloy structure. As a result, forming HEAs of multiple principal elements is not guaranteed, even though the increased mixing entropy always positively contributes to the uniform mixing. For instance, the combinations of elements with highly positive values of ΔH_{ij} (i.e., dominated by strong repulsive forces, for example, Au-Ni, Au-Pt, etc.) exhibit immiscibility, usually leading to phase segregation. The combinations with highly negative values of ΔH_{ij} (i.e., dominated by strong attractive forces, for example, Pt-Ni, Pt-Sn, etc.) favor structural ordering, forming intermetallic phases.[3] The mixing entropy becomes dominant to promote homogeneous and random element mixing and HEA formation only when all ΔH_{ij} pairs are close to zero (i.e., weak repulsion or attraction). However, the significant

physicochemical differences among different metal elements result in a wide range of ΔH_{ij}, making the homogeneous mixing thermodynamically nonspontaneous and challenging. Phase-segregated (i.e., multiple domains with different crystalline phases) and composition-segregated (multiple domains with different compositions) structures are more typical for the alloys of multiple principal elements synthesized from the near-equilibrium approaches. Therefore, implementing kinetic control represents a solution to tackle this challenge, enabling the synthesis of HEAs.

A high temperature increases the contribution of mixing entropy to homogeneously mixing multiple elements and minimizes the ΔH_{ij} difference of different elemental pairs due to the weakening of metallic bonds at a high temperature, particularly near or above melting temperature. For example, at a temperature above the melting points of multiple elements, a liquid solution of these elements can be easily generated to enable a homogeneous mixing due to the significantly enhanced diffusivity of atoms in the liquid phase and high temperature. Solidifying the liquid solution at different cooling rates leads to a solid phase with different structures, indicating the importance of solidification kinetics. The typical metallurgic time-temperature-transformation (TTT) diagram (Figure 1A) shows that the kinetic formation of metallic glass, HEA, and phase-segregated structures from a supercooled liquid alloy strongly depends on the cooling rate during solidification of the liquid alloy.[4] A rapid-enough temperature quenching is necessary to retain the high-entropy mixing state of a liquid metal and yield single-phase HEA by avoiding the TTT nose. When the cooling rate drops, crystalline phase separation, usually associated with composition segregation, occurs to form a heterogeneous phase-segregated alloy (right side). In contrast, metallic glass is formed by maintaining the amorphous phase of the metal liquid as the cooling rate is superfast (left side). The TTT diagram highlights the crucial role of cooling rate in forming single-phase HEAs from liquid metal alloys and provides the guideline for selecting the appropriate cooling rate. Once the single-phase HEAs are formed at lower temperatures, the contribution of mixing entropy ($-T\cdot\Delta S_{\mathrm{mix}}$) to the system Gibbs energy lowers due to the temperature decrease, making the HEAs less thermodynamically stable. However, transforming a single-phase HEA to a thermodynamically more stable phase-segregated alloy involves significant diffusion of metal atoms in the HEA, which is a kinetic-controlled process. Sluggish diffusion kinetics in a HEA is important to maintaining stability and outstanding properties even at room temperature. Figure 1B compares the diffusion coefficient of an element in different face-centered cubic (fcc) lattices of various compositions, showing the influence of composition on atom

diffusion.[5] Regardless of the nature of the element (e.g., Cr, Fe, and Ni), their diffusion kinetics slows with increasing number of elements in the lattices. The diffusion coefficients in the CoCrFeMnNi HEA are consistently lower than those in ternary alloys and pure metals, and the difference is more pronounced at lower temperatures. The results in Figure 1B provide direct evidence for the sluggish diffusion effect in HEAs. An alloy lattice containing more elements has a greater fluctuation of lattice potential energy that produces more significant atomic traps and blocks to account for the sluggish diffusion in HEAs.

The metallurgic TTT diagram and sluggish diffusion effect in HEAs suggest that successful synthesis of HEAs requires homogeneous mixing of the atoms of all constituent elements followed by solidification and crystallization at an appropriate fast-enough cooling rate. Despite the thermodynamic term "high entropy" is always highlighted in HEAs and related research, the success of synthesizing HEAs heavily relies on kinetics control over mixing atoms of different elements, crystallizing the homogeneously mixed atoms, and minimizing the diffusion of atoms in HEAs to avoid phase segregation. In the past five years, the HEA research was dominated by synthesizing HEA nanoparticles and their applications in energy-related fields, including catalysis,[6-15] electrochemical energy storage,[11, 16-20] and light harvesting and conversion.[21-26] The emergence of HEA nanomaterials and their promising properties have attracted extensive attention and resulted in some review articles primarily focused on catalysis.[8, 9, 11-14] Although the synthesis of HEA nanomaterials is crucial to exploring their unique properties, a focused and insightful overview of synthetic strategies is still rare in literature. Some review articles provide brief collections of the synthesis methods of different names defined in the individual original work, while the significant portions of these articles focus on properties and applications. Most recently, several review articles have been published emphasizing the synthesis and fabrication of HEA nanomaterials.[27-29] There is no discussion on the shared commonality and significant distinction among different synthesis methods. Therefore, this review will focus on understanding all the differently "named" methods reported for synthesizing HEA nanoparticles to provide generalized principles that can link the methods of different names with sharing the same rationales. First, the synthesis strategies of various general principles will be categorized and discussed in detail to highlight their capability in synthesizing single-phase HEA nanoparticles. Second, the reported typical synthesis methods sharing the same principles will be examined and discussed. Finally,

personal perspectives on the development of HEA nanoparticle synthesis will be concluded to demonstrate the potential interest of the related fields.

2. Strategies for Synthesizing Metallic HEA Nanoparticles

Similar to the methods developed for synthesizing nanomaterials in the past decades, two complementary pathways, including top-down (physical) minimization and bottom-up (chemical) synthesis, can be applied to synthesizing metallic HEA nanoparticles. The top-down strategy relies on various methods to break down the already-manufactured HEA metal ingots into nanometer-sized particles. The bottom-up strategy starts with producing metal atoms of all constituent elements from the corresponding metal precursors in a homogeneous mixing. This mixing step is followed by controlled crystallization to maintain the homogeneous mixing of different atoms and keep the crystal sizes at the nanometer scale.

Figure 2 summarizes the typical methods of physical minimization of bulk metals, including HEAs, simple alloys, and pure metals. Many HEAs have been successfully manufactured following the techniques developed according to the metallurgic TTT diagram in Figure 1A. When a HEA metal is minimized into nanoparticles, the surrounding temperature must remain low enough to prevent diffusion of individual elements within the HEA and maintain the single HEA phase in the resulting nanoparticles. For example, a HEA metal ingot can be shredded or fragmented into small pieces at room temperature (Figure 2A, step i). The small HEA pieces are then vigorously milled to break them further into nanoparticles (Figure 2A, step ii). It is crucial to keep the mechanical milling process at a much lower temperature because the excessive heat generated from the vigorous milling has to dissipate to avoid temperature elevation in the HEA lattices quickly. A typical example is cryo-milling, in which the temperature of the milling vial is controlled by a cryogenic liquid (e.g., liquid nitrogen). When diffusion of metal atoms is necessary to mix them homogeneously to form HEA nanoparticles, milling at ambient conditions is preferred because the impact energy deposited by the milling ball can significantly increase the temperature of the milling metal powders to promote atomic diffusion. A processing medium (i.e., a liquid solvent such as toluene) is usually used to prevent cold fusion of the fragmented particles, facilitating the continuous decrease of particle size during milling. The resulting nanoparticles can be dispersed in a solvent containing capping agents, where they can be well-separated to prevent agglomeration and fusion. Moreover, a piece of HEA metal can be heavily compressed into a sheet

with a thickness down to a nanometer scale due to its good ductility (Figure 2A, step 1).[30] The thin sheet is then patterned with a resist layer followed by an appropriate lithographic process to produce nanostructures with desired sizes and shapes (Figure 2A, step 2). Selectively etching the area uncovered with the resist, regardless of wet chemical etching or dry plasmon etching, should not significantly increase temperature, avoiding the possible phase segregation in the resulting nanostructures due to diffusion of atoms. The methods summarized in Figure 2A are labeled "*Physical Minimization of HEA Metals*" in this article.

The physical minimization can also start with metals of pure elements and/or alloys containing the constituent elements of the HEA nanoparticles of interest. The first step is to vaporize metal atoms from the metal targets with appropriate conditions and stimuli (Figure 2B, step i). For instance, in a high-vacuum chamber, all targets can be atomized simultaneously using a focused high-power source, such as a direct-current (DC) magnetron field and electron beam. Still, each target is atomized independently to allow the vaporization rate of each element to match its concentration in the synthesized HEA nanoparticles. In addition to the bombardment techniques, high-temperature plasma can also vaporize metals with vaporization rates depending on their boiling points. The atomic vapor pressure of one metal element is determined by the plasma temperature (power) and its concentration in the metal target. The fraction of one element with a high boiling point in the metal target should be much higher than that of a low-boiling-point element to achieve comparable vapor pressures (or vapor concentrations). All elements of the synthesizing HEA nanoparticles should be carefully mixed in the metal targets, which are used as electrodes (cathode or anode) for electrical discharging to generate high-temperature plasma in an appropriate gas atmosphere. The vaporized metal atoms quickly mix into a homogeneous cloud because of their fast diffusivities in the gas phase. The well-mixed metal atoms will then condense and crystallize into HEA nanoparticles in an appropriate dispersion medium or on a support substrate, which remains at a low temperature (e.g., room temperature) (Figure 2B, step ii). The temperature should be low enough to allow all gas-phase atoms to condense simultaneously into solids while maintaining the homogeneous mixing. The following crystallization forms single-phase HEA that is kinetically stable. The liquid dispersion medium behaves like a capping reagent to stabilize the nanoparticles or contain surfactants to achieve this function, keeping the HEA nanoparticles well separated and dispersed. The plasma gas can also be a dispersion medium to carry the produced HEA nanoparticles, forming an aerosol. The appropriate support substrate

should have a surface with nonuniform affinities that can promote localized nucleation and growth of HEA nanoparticles to avoid the formation of a continuous film. The method summarized in Figure 2B is labeled "*Vaporization of Metals*" in this article, which involves both a top-down step (i.e., atomization) and a bottom-up step (i.e., condensation and crystallization of homogeneously mixed atoms).

Metal atoms can be generated from their corresponding precursors, including ionic salts and organometallic compounds, through chemical reduction and/or thermal decomposition that is equivalent to a disproportionation reaction. Under suitable reaction conditions, the metal atoms of different elements can also be homogeneously mixed to enable the formation of single-phase HEA nanoparticles. This strategy represents the traditional bottom-up chemical synthesis. When using metal ions as example precursors, three approaches are sketched in Figure 3 depending on the characteristics of precursors and reaction conditions. The crucial step of the bottom-up strategy is generating homogeneously mixed metal atoms with compositions similar to those in the final HEA nanoparticles. When the metal precursors of different elements are homogeneously dissolved in a reaction solution, the reductant must be strong enough to reduce all metal ions simultaneously at a high rate to maintain the homogeneous mixing of metal atoms to initiate homogeneous nucleation (Figure 3A). The HEA-like nuclei will grow by spontaneously condensing and crystallizing the well-mixed metal atoms into HEA nanoparticles dispersed in the solvent containing a capping reagent that stabilizes the nanoparticles. The reaction temperature is usually mild, i.e., lower than the boiling point of the solvent, and does not significantly promote diffusion of different atoms. Therefore, the single-phase HEA nanoparticles will be stable once formed from the reaction solution. Thermal annealing at an appropriate temperature might be necessary to increase crystallinity of the nanoparticles. The method summarized in Figure 3A is labeled "*Burst Reduction*" in this article.

When the synthesis starts with solid metal salts (or dried metal salt solution on granular support), the metal ions of different elements usually do not have uniform spatial distributions, which is different from the liquid solutions. Mild-temperature reduction of these metal ions in the solid salt crystals cannot homogeneously mix the resulting metal atoms due to the limited diffusivity in the solid phase. In contrast, the diffusivity of metal atoms in the liquid phase at high temperatures above their melting points increases dramatically to enable fast mixing of all metal atoms. Therefore, a thermal shock that provides a pulsed high temperature for a short duration

becomes necessary to decompose all metal precursors into metal atoms and melt the resulting metals into a homogeneous mixture. The importance of the short duration of the thermal shock is to selectively elevate the temperature of metals but not the surrounding environment (e.g., atmosphere) that remains cool. Once the thermal shock is turned off, the large temperature gradient of the melted metals with respect to the support substrate and the gas atmosphere can quickly cool down the metals to freeze/crystallize them into nanoparticles with uniform element distribution (i.e., single-phase HEA nanoparticles) (Figure 3B). The flash heating and cooling involved in thermal shock are similar to the typical TTT diagram of Figure 1A, which describes the fabrication of solid-solution single-phase HEAs. The cooling rate is crucial to determine the formation of HEA crystalline phase. In order to shatter the melted metals into HEA nanoparticles on the support, the support surface should exhibit a non-uniform affinity toward the metals to facilitate heterogeneous nucleation of the HEA nanoparticles only on the affinitive sites. The spatial separation of nucleation sites enables the resulting HEA nanoparticles to be well dispersed on the support rather than fused into large agglomerates. The method summarized in Figure 3B is labeled "*Thermal Shock*" in this article. The thermal shock method can also apply to the alloy metal nanoparticles that do not have a homogeneous mixing of all atoms. The flash heating melts the nanoparticles to mix the metal atoms homogeneously, and the following flash cooling re-crystallizes the atoms into single-phase HEA nanoparticles.

When the reduction of metal ions is not performed under the previous extreme conditions (i.e., with burst reduction or thermal shock), the metal atoms reduced from the ions may not directly condense and crystallize into single-phase HEA nanoparticles because of their different reduction rates and immiscibility. The widely explored method for colloidal nanoparticle synthesis is solvothermal reduction, which allows the temperature to be above the boiling point of the solvent and pressure higher than the standard atmosphere. The elevated temperature, even below the metal melting point, can promote the diffusivity of metal atoms in the growing nanoparticles, in which only short diffusion distances are needed to homogeneously mix all elements due to the small size of nanoparticles. Maintaining the solvothermal conditions for a long enough period can synthesize single-phase HEA nanoparticles with solid-solution mixing of all elements regardless of their miscibility. The difference in reduction potentials of metal precursor ions (corresponding to different reduction rates) and supersaturation for nucleation may lead to homogeneous nucleation that involves only one or two elements. The nuclei then autocatalyze the simultaneous reduction

and precipitation of all metals at rates with a constant ratio to grow the nanoparticles (Figure 3C, top). If the immiscibility of different elements is severe, sequential multiple steps can be employed to reduce metal ions, forming core-shell nanoparticles. The cores and shells have well-defined compositions (e.g., either alloy or single element). Compared to the growing nanoparticles, the diffusion distances of atoms in the synthesized core-shell nanoparticles are much more significant to complete homogeneous mixing. Therefore, a much higher temperature than solvothermal synthesis is necessary to anneal the synthesized core-shell nanoparticles, promoting the interdiffusion of atoms between the cores and shells to drive the formation of single-phase HEA nanoparticles (Figure 3C, bottom). The high-temperature annealing is usually performed in an inert gas atmosphere (or reducing atmosphere) to avoid side reactions that degrade the nanoparticles. Specifically, the core-shell nanoparticles are loaded to a support substrate, on which the nanoparticles have appropriate interaction/affinity with the substrate to prevent potential fusion or agglomeration of the nanoparticles during thermal annealing. The annealing usually avoids melting the nanoparticles. Once the interdiffusion mixes the core and shell of each nanoparticle, the high mixing entropy stabilizes the HEA phase and crystalline structure even at the annealing temperature. The cooling process will not change the HEA phase and is not sensitive to the cooling rate, so no flash cooling is necessary. If the interdiffusion between the cores and shells is too slow at temperatures below their melting points, thermal shock presented in Figure 3B becomes necessary to transform the core-shell nanoparticles into single-phase HEA nanoparticles. The methods summarized in Figure 3C are labeled "*Solvothermal Reduction and Annealing*" in this article.

3. Physical Minimization of HEA Metals

Many HEA cast ingots have been fabricated from the combinations of corresponding metals by following the TTT diagram of Figure 1A. These HEA ingots can be pulverized into nanoparticles using ball milling at extremely low temperatures. Kumar and co-workers demonstrated the feasibility and promise of cryo-milling in synthesizing HEA nanoparticles.[31] The high ductility and toughness, for example, a face-centered cubic (fcc) HEA phase possessing a ductility of >40% and toughness of >250 $MPa \cdot m^{1/2}$, represent the challenges to crush HEA ingots into nanoparticles because of the easy cold welding. However, the advantages of cryo-milling, including low contamination, restricted oxidation, and suppression of recovery and

recrystallization at an extremely low temperature (e.g., −196 °C in liquid nitrogen), make it promising to tackle the challenges and enable the scalable synthesis of HEA nanoparticles. Figure 4A presents the typical setup of a cryomill that must have the key features: (i) separation of cryogenic liquid from metal powder, (ii) prevention of the milled metal powder from oxidation and/or nitridation using inert atmosphere (e.g., Ar) in the vial, (iii) control over the temperature of the milling powder in the course of ball milling, and (iv) visualization of the milling process to estimate the impact energy transferred to the powder.[32] Single-phase fcc HEA ingots with equimolar compositions (i.e., FeCrMnNiCo, CuAgAuPtPd) and single-phase body-centered cubic (bcc) HEA ingots of FeCrMnVAl were fabricated using arc melting of high-purity element metals under protection of Ar, followed by homogenization at 1000 °C for 10 h casting. These HEA ingots were first sliced into small pieces using a diamond saw. The small HEA pieces were then milled in the cryomill (Figure 4A) at −160 ± 10 °C using liquid nitrogen as the cryogenic liquid, while the milling chamber was constantly purged with high-purity Ar. Continuous milling for 6 h usually produced HEA nanoparticles from their corresponding HEA ingots. The X-ray diffraction (XRD) patterns of the FeCrMnNiCo HEA ingot and the as-synthesized nanoparticles are compared in Figure 4B. Both samples share the same set of XRD peaks, indicating that the single fcc HEA phase is maintained in the nanoparticles after cryo-milling. The XRD peaks of the nanoparticles become broader than those of the ingot (inset, Figure 4B), consistent with the size reduction to the nanoscale. Lattice strain induced from the cold processing and the intrinsic lattice distortion due to different atom sizes of different elements also contribute to the broadening of XRD peaks. Figure 4C shows a typical transmission electron microscopy (TEM) image of the as-synthesized FeCrMnNiCo HEA nanoparticles with an average size of 4 ± 1 nm (inset). Although individual nanoparticles in the powder seem to stick together (or be welded), they can be well dispersed in a solvent, particularly in the presence of a capping agent, such as oleylamine, after ultrasonication. The fcc CuAgAuPtPd and bcc FeCrMnVAl nanoparticles exhibit similar characteristics to the fcc FeCrMnNiCo HEA nanoparticles. Figure 4D displays a TEM image of the CuAgAuPtPd nanoparticles prepared after being dispersed in a solvent, showing the presence of individual nanoparticles spread on the TEM grid and their average size of 16 ± 10 nm.[33] High-resolution scanning transmission electron microscopy (HR-STEM) image of a single nanoparticle along [001] crystallographic direction reveals the lattice with varying contrasts that could be assigned to atoms of different elements (highlighted with different colors in the inset, Figure 4D). The randomly

homogeneous distribution of all elements in the well-defined fcc lattice confirms their single HEA phase. The atom probe tomography (APT) images of the five elements exhibit similar intensity profiles in the probed space, highlighting their homogeneous mixing in single nanoparticles (Figure 4E). The X-ray photoelectron spectroscopy (XPS) characterization, a surface-sensitive technique, shows that CuAgAuPtPd nanoparticles possess surfaces with a chemically homogeneous HEA. The HEA surfaces can be considered a "single-atom catalyst", for example, the Cu atoms stabilized by other metal atoms in the fcc crystalline structure, to achieve better performance in catalyzing reactions of interest. The single-phase CuAgAuPtPd HEA nanoparticles can electrochemically catalyze the reduction of CO_2 to gaseous hydrocarbons with an approximate unity Faradic efficiency at a low cathodic potential, i.e., –0.3 V vs. reversible hydrogen electrode (RHE). A low-cost oxygen evolution reaction (OER) catalyst with a HEA composition, i.e., CoFeGaNiZn, was also synthesized using the cryo-milling technique.[34] The synthesized nanoparticles exhibit a single-phase HEA with fcc lattices and an average size of 8 ± 4 nm. The cyclic voltammetry activation can oxidize the surfaces of the CoFeGaNiZn HEA nanoparticles into high entropy (oxy)hydroxides, which exhibit a low overpotential of 370 mV at a current density of 10 mA/cm^2 and a small Tafel slope of 71 mV/dec.

The typical characteristics of single-phase HEA nanoparticles shown in Figure 4A-E, including nanoscale size, well-defined single crystalline phase, and random and homogeneous distributions of each element from the center to the surface in individual nanoparticles, shed light on the promise of cryo-milling of HEA ingots in synthesizing HEA nanoparticles. The extremely low temperature is crucial to prevent the diffusion of atoms, particularly non-uniform diffusion of different atoms, in the HEA lattices during the milling process, inheriting and maintaining the single HEA phase from the original HEA ingot. The low temperature might help harden the small HEA pieces and make them brittle, facilitating them to be pulverized into nanoparticles by overcoming the welding problems.[35] In contrast, the temperature of milling powder increases without the cryogenic liquid because the impact energy of the ball can transfer to the powder. The elevated temperature will increase the diffusivity of atoms in the milling powder. Therefore, HEA nanoparticles could be directly synthesized from pure metals by milling the high-purity metals of all elements at the molar ratios same as the nanoparticles. Figure 4F shows the evolution of XRD pattern of the milling powder started from high-purity Al, Fe, Ti, Cr, Zn, and Cu powders (≤45 μm) in equiatomic ratio.[36] No cryogenic liquid cooling was applied to the mill system, and toluene was used as a process-

controlling agent. The number of XRD peaks from six different metals decreases with milling time, and the number at 20 h reduces to a pattern consistent with a single bcc phase, indicating the formation of single-phase hexanary AlFeTiCrZnCu HEA powder. Significant peak broadening is also observed due to the formation of nanocrystallites and lattice strains. TEM image of the milled powder confirms the production of nanoparticles with sizes around 10 nm (inset, Figure 4F). Energy dispersive X-ray spectroscopy (EDS) microanalysis of the nanoparticles verifies the equiatomic composition and homogeneous distribution of all elements. HEA nanoparticles made of binary AlFe, ternary AlFeTi, quaternary AlFeTiCr, and quinary AlFeTiCrZn were also synthesized using the same milling process but at shorter times. The slower interparticle diffusivities could be responsible for the longer milling time needed to form single-phase HEA in systems with a larger number of elements. Although synthesizing HEA nanoparticles by directly milling pure metal powders is simple, the longer milling time usually causes potential contamination and oxidation. Soft magnetic FeCoNiCrAl HEA nanoparticles were also synthesized by milling the corresponding pure metal powders for 12 h.[37] When the pure metal powders are mixed with other constituents in the mill vial, composites of HEA nanoparticles on granular supports can be synthesized after milling. For example, using mechanical milling, Rekha and co-workers synthesized NiFeCrCoCu HEA nanoparticles dispersed on graphene nanosheets.[38] High-purity graphite powder was milled with metal powders of these five elements in toluene for 80 h, forming a metal-graphite composite with HEA metal nanoparticles intercalated in the graphene interlayer gaps. The graphite (002) XRD peak shifted to a lower angle, indicating the expansion of the interlayer distance due to the formation of HEA nanoparticles. The composite can be dispersed in an ethanolic solution of sodium lauryl sulphate with assistance of sonication for 2 h, leading to the exfoliation of graphene sheets decorated with the HEA metal nanoparticles. Figure 4G shows a typical TEM image of the graphene-supported HEA nanoparticles with an average size of 8 ± 2 nm. The electron diffraction analysis indicates that the HEA nanoparticles are crystallized into fcc lattices with lattice constant of 3.394 Å. STEM-EDS analysis was used to study the distribution of all elements in individual nanoparticles through both compositional mapping and line-scan. Figure 4H compares the line-scan profiles of the five elements (i.e., Cr, Co, Ni, Cu, and Fe) of a representative HEA nanoparticle (inset). The high level of their overlap confirms the uniform distribution of different elements in the nanoparticles. The HEA

nanoparticle/graphene composite exhibits superior corrosion resistance to milled and exfoliated graphene, which is promising for corrosion resistant coating applications.

In summary, mechanical milling is a powerful technique to pulverize metal powders into nanoparticles, regardless of their compositions. The "cold" cryo-milling favors the scalable synthesis of HEA nanoparticles from HEA ingots with the same compositions because the slow solid-state diffusion of atoms is unnecessary. The "hot" ambient milling can promote the solid-state interdiffusion of different atoms to form HEA nanoparticles from pure metals, but the synthesis usually takes much longer to allow mixing all metal atoms uniformly in individual nanoparticles. Although cryo-milling is preferred for synthesizing freestanding HEA metal nanoparticles, the ambient milling can synthesize composites containing HEA metal nanoparticles. As described in Figure 2A, compressing HEA metals into ultrathin sheets without changing the crystalline phase is feasible because of their high ductility and toughness. The thin sheets can be patterned with appropriate resist followed by selective etching, forming HEA nanoparticles. Such lithographic process has been widely used in fabricating metal nanoparticles from thin metal films.[39] This strategy could be ready to synthesize HEA nanoparticles once ultrathin HEA sheets are ready to fabricate.

4. Vaporization of Metals

Atomization (or vaporization) of metals usually requires a vacuum or low pressure to ensure the metal atoms of different elements mix homogeneously and avoid contamination before they condense and crystallize into HEA nanoparticles. Breaking metallic bonds to convert a metal solid (e.g., ingot, rod, and powder) into gaseous atoms needs a large energy input that extremely high temperatures can achieve. For example, magnetron sputtering in a vacuum chamber can bombard metal targets to vaporize metal atoms. At a position away from the sputtering source, the metal atoms can condense and be collected as new solids (either films or nanoparticles) depending on the characteristics of the receiving medium. Multiple high-voltage magnetron generators can be equipped in a vacuum chamber and operated independently to control the atomization rate of each metal target. Figure 5A illustrates the configuration of an ultrahigh-vacuum (UHV) deposition system with five confocal cathodes that allow simultaneous atomization of up to five different metal targets. The high kinetic energy of vaporized metal atoms carried from sputtering excitation enables them to instantaneously mix into homogeneous metal clouds, which are ready to condense

into a solid alloy on an appropriate receiving substrate for the formation of uniform film or in a non-volatile solvent for the synthesis of dispersed nanoparticles. Ionic liquid with a low melting point and negligible vapor pressure represents an ideal choice for synthesizing HEA nanoparticles using the multiple-target co-sputtering system. The ionic liquid is transferred by a load-lock from the high-purity Ar atmosphere (storage environment) to the UHV chamber, maintaining its clean and moisture-free state to avoid the interference of the UHV condition and contamination of the synthesized nanoparticles. Löffler and co-workers used multiple cavity holders (stainless steel) for carrying ionic liquid, in which the metal atoms condensed into nanoparticles.[40] Since the atom vapor generated from each target is a somehow focused beam, the deposition flux varies with the relative angle of the receiving ionic liquid cavity. In combination with the independent tunability of the vaporization rate of each metal target, the configuration of Figure 5A provides great promise in the combinatorial synthesis of HEA nanoparticles with tunable compositions in an extensive library.[41] For instance, there are more than two million possible combinations for quinary alloys selected from a list of 50 elements, and each combination can have tunable compositions (i.e., different concentrations of different elements). Figure 5B presents a TEM image of the quinary CrMnFeCoNi HEA nanoparticles with nearly equimolar composition synthesized from co-sputtering of five individual high-purity metal targets in 1-butyl-3-methylimidazolium bis(trifluoromethyl sulfonyl) imide ([Bmim][Tf_2N]). The nanoparticles are stabilized by the ionic liquid and exhibit an average diameter of 1.7 ± 0.2 nm (right inset, Figure 5B). The fast Fourier transform of the TEM image (left inset, Figure 5B) and diffraction patterns do not show observable lattice reflections, indicating that the nanoparticles are amorphous or low quality in crystallinity. Each element's EDX mapping shows a similar spatial intensity profile, indicating the homogeneous distribution of all five elements in individual nanoparticles, consistent with typical HEA features. Quaternary HEA nanoparticles (e.g., MnFeCoNi, CrFeCoNi, CrMnCoNi, CrMnFeNi, and CrMnFeCo) synthesized from the same system have larger sizes in the range from 3.0 to 3.7 nm, exhibiting better crystallinity. The size of nanoparticles can also be tuned by employing different ionic liquids.[42] Due to the high cost and high viscosity of ionic liquids, the HEA nanoparticles synthesized in the ionic liquids need to be precipitated out by adding a capping agent (e.g., 1-dodecanthiole)[43] or transferred to traditional solvents by adding acetonitrile containing a small amount of appropriate organic surfactants.[41] Quinary CoCrCuFeNi HEA nanoparticles with complex magnetic properties were also synthesized in an ionic liquid of 1-butyl-

3-methylimidazolium tetrafluoroborate ([Bmim][BF_4]) using the magnetron sputtering technique.[44]

Unlike magnetron sputtering requiring high vacuum, arc discharge in a chamber filled with an appropriate gas can generate plasma with extremely high temperatures to vaporize metals. Figure 5C shows the setup configuration of a typical arc plasma chamber.[45] Electric arc occurs between a sharp carbon (e.g., graphite) cathode and a metal target anode due to discharge when these two electrodes are close enough and/or the applied voltage is high enough. The electric arc can ignite the gases to generate high-temperature plasma around the metal target, leading to the vaporization of metal atoms from the metal target. The atom vaporization rate depends on the element's boiling point, and the metal with a higher boiling point usually exhibits a slower vaporization rate and a lower vapor pressure in the chamber upon arc discharge. The metal target anode in an arc-discharge system needs to contain all elements of the desired nanoparticles, although the geometry of the metal target can be versatile. For instance, the synthesis of quinary **ABCDE** HEA nanoparticles requires a uniform mixture of five different metal powders of **A**, **B**, **C**, **D**, and **E**, which can be compressed into a pellet or a cylinder. A uniform mixture of metal powders of pure elements or alloys (e.g., **A**, **B**, **C** elements, and **DE** alloy) is also appropriate for being an anode. Liao and co-workers reported the use of the arc-discharge method to synthesize HEA nanoparticles made of up to 21 metal elements, including Fe, Co, Ni, Cr, Y, Ti, V, Cu, Al, Nb, Mo, Ta, W, Zn, Cd, Pb, Bi, Ag, In, Mn, and Sn.[26] The chamber was first vacuumed to 5 mPa after installing the cylinder-shaped metal target anode. The reaction gases of Ar and H_2 were then introduced into the chamber to a pressure close to the ambient pressure (i.e., 1 atmosphere) for convenience. Continuously operating the arc-discharge process for 5-10 minutes evaporated enough metal atoms to produce HEA nanoparticles on the cooling collection plate that was set at either 300 K (cooled by water) or 150 K (cooled by liquid nitrogen). HEA nanoparticles made from 3, 5, 7, 9, 13, 17, and 21 metal elements of various combinations were successfully synthesized. The elemental composition in a sample is controlled by the molar ratio of metal powders of each element, considering varying vapor pressures of different elements originating from their different boiling points. For example, the low vapor pressures of Ti and V lead to relatively lower molar fractions than other constituent elements in the FeCoNiTiVCrCu HEA nanoparticles when the molar fractions of all elements in the target anode are the same. Carefully increasing the fractions of Ti and V powders in the target anode elevates their concentrations in the HEA nanoparticles to the desirable values. The 21

element metals used in this work could be classified into three groups: (i) low vapor pressure metals (Mo, Nb, Ta, W), (ii) medium vapor pressure metals (Fe, Co, Ni, Y, Ti, V, Al, Cu, Cr, Sn) with Sn, Al, Cu in the upper range and Ti, V in the lower range, and (iii) high vapor pressure metals (Ag, Mn, In, Pb, Bi, Zn, Cd). This classification helps prepare the metal target anodes with the appropriate compositions to synthesize HEA nanoparticles with the desirable compositions. Equiatomic FeCoNiCrYTiVCuAl HEA nanoparticles were synthesized from the target anode containing 10-time Ti and V and 0.5-time Cu and Al compared to other constituent elements. Optimizing the evaporation rate of the low vapor pressure metals is crucial for alloying the immiscible combinations into single-phase HEA nanoparticles. In work reported by Mao and co-workers,[46] the metal target of $Co_aCr_bCu_cFe_dNi_e$ was used to synthesize HEA nanoparticles made of the composition of $Co_aCr_{3b}Cu_{12c}Fe_{1.5d}Ni_e$, confirming the influence of different vapor pressures on the composition of nanoparticles. It is worth noting that the crystalline structures change from fcc to bcc as the number of constituent elements in the HEA nanoparticles is larger than nine (Figure 5D). The XRD peaks of high-number HEA nanoparticles become broader and shift to lower 2θ values, which could be ascribed to lattice distortion and inclusion of large-size atoms (e.g., Ta, W, Pb, and Bi). All elements in individual HEA nanoparticles are homogeneously mixed regardless of their compositions. The EDS maps of each element in the 21-element FeCoNiCrYTiVCuAlNbMoTaWZnCdPbBiAgInMnSn HEA nanoparticles exhibit the very similar spatial distribution profiles, confirming the homogeneous mixing of all elements in the nanoparticles. The as-synthesized HEA nanoparticles exhibit broadened absorption bands of light due to extensive interband transitions, making them a promising class of efficient photothermal conversion materials for applications like water purification and desalination.[25, 26] When the reaction gas contains CH_4 that can be decomposed to C in the plasma, core-shell nanoparticles containing HEA nanoparticle core and C shell will be synthesized. Microwave-absorption materials of FeCoNiTiMn HEA@graphite core-shell nanoparticles and photothermal conversion materials of FeCoNiTiVCrMnCu@graphite core-shell nanoparticles were synthesized and studied.[25, 47]

When the arc discharge occurs between two electrodes with a cylinder shape by applying a power source that generates harmonic oscillation at a frequency of MHz, more efficient vaporization/mixing of atoms and HEA nanoparticle synthesis can be realized. Figure 6A presents the working mechanism of the “sparking mashup” vapor-source technique that provides an

unrestricted mixing environment for synthesizing HEA nanoparticles.[48] The capacitor in the power source circuit is parallel to the pair of cylinder electrodes (i.e., metal targets) separated by a small gap (usually less than 0.5 mm). An ambient-pressure flow of H_2/Ar gas flushes the electrode gap, and discharge sparks form between the electrodes when the voltage over the capacitor reaches the gas breakdown threshold. The subsequent charging process is then restarted, followed by discharging. Repetition of such a charging-discharging cycle generates "spark oscillation". The alternate polarity reversal makes the electrodes take turns to behave as the momentary cathode, which is ablated due to cation bombardment. As a result, atomic vapors from both electrodes can be generated in a single spark oscillation. Once a spark plasma in the electrode gap is triggered, it expands and repels the surrounding gas to create a low-pressure region that pulls the metal vapors injected from different electrodes upon oscillatory sparking within a duration of microseconds. The vapor jets undergo ballistic transport toward each other ($>10^3$ m·s^{-1}) to enable ideal mixing at a high temperature and low pressure. In order to generate a concentrated and directional flow of metal vapor, the two electrodes of different materials are made in the shape of a wire and a cylindrical tube (Figure 6B). The gas flows towards the tube to carry the homogeneous metal vapor into the tube, in which the metal atoms nucleate and condense to form HEA nanoparticles dispersed in the carrying gas. The aerosol can be directly collected in the downstream. The electrode material can be a pure metal or an alloy, depending on the composition of the interesting HEA nanoparticles. For instance, an **ABC** alloy wire and a **DE** alloy tube can synthesize **ABCDE** HEA nanoparticles upon "sparking mashup". The amount of current flowed as positive and negative polarity in an oscillating spark defines the vapor composition translated to the HEA nanoparticles. The gap between the two electrodes is an important parameter for determining the spatial distribution of metal vapors. The gap should be small enough to allow homogeneous vapor mixing while preventing material transfer between the two electrodes. Since metallic bonding is electronic in nature and underlies quantum physical effects, the "sparking mashup" method enables the homogeneously alloying of any dissimilar and immiscible metals in nanoparticles.[48] Intermetallic phases can be kinetically suppressed, and random alloys (i.e., HEA phases) are promoted. Feng and co-workers used the "sparking mashup" method to synthesize 55 distinct alloy nanoparticles with sizes of < 5 nm by strongly diluting the aerosol followed by immobilizing the nanoparticles onto a substrate through aerosol deposition via filtration or electrical attraction.[48] Figure 6C (top left panel) shows a high-angle annular dark-field (HAADF) aberration-corrected (Cs) STEM

image of a HEA nanoparticle made of six elements (NiCrCoMoAuAg), clearly displaying the feature of a single crystalline phase. The blurring of the image is related to the inherent drifting problem for such minuscule nanoparticles. The Cs-STEM EDS maps of individual elements of one representative nanoparticle overlap very well (Figure 6C), indicating the homogeneous mixing of all six elements in the nanoparticle. The microscale compositional analysis is consistent with the macroscale analysis determined by inductively coupled plasma mass spectrometry (ICP-MS). These characterizations confirm that the nanoparticles synthesized from "sparking mashup" adopt the single HEA phase with random alloying. Moreover, spark mashup also generates gaseous ions along with the mass production of singly charged nanoparticles, preventing nanoparticle agglomeration in the flowing aerosol. An external electric field can control the movement of these nanoparticles due to the charges. The small sizes of the synthesized HEA nanoparticles make them a potential class of building blocks for three-dimension (3D) printing (or additive manufacturing). For example, a dielectric substrate with appropriate patterns holding opposite charges can be used as a fundamental component to reconfigure electric field lines into "funneling channels" to precisely guide the movement of the directly synthesized charged HEA nanoparticles. The nanoparticles settled on the received substrate exhibit ordering energy at least two orders of magnitude higher than the kinetic energy of Brownian motion at room temperature, maintaining the condensed packing of nanoparticles in the 3D structures. Figure 6D (top panels) presents the SEM images of the 3D flower-like structures printed from the senary NiCrCoMoCuPd HEA nanoparticles.[48] These 3D structures are formed on a patterned dielectric layer of poly(methyl methacrylate) (PMMA) on the surface of a conductive doped Si wafer. The EDX mapping (Figure 6D, bottom panels) confirms that the 3D structures retain the alloyed states of the HEA nanoparticles. Additional annealing may sinter the HEA nanoparticles to further solidify the 3D structures into denser HEA structures, improving the HEA characteristics in the 3D structures.[36] Wu and co-workers[49] also used the sparking mashup method for synthesizing HEA nanoparticles made of CoCrFeNiPt and $CoFeNiCr_{0.5}Pd_{0.8}$ and Suliz and co-workers[50] for synthesizing AlCrFeCuNi HEA nanoparticles.

In addition to electric discharge, plasma can also be generated by shinning a high-power pulsed laser on a metal surface to ablate the metal target, forming nanoparticles. The laser ablation nanoparticle synthesis can be performed in both gas (including vacuum) and liquid medium, and even at the gas/liquid interface. The formation of HEA nanoparticles in the gas phase is similar to

the arc discharge methods. In a typical synthesis of colloidal HEA nanoparticles in a liquid, a pulsed laser beam of sufficient energy fluence irradiates the surface of a bulk HEA target, forming a plume. A cavitation bubble is sequentially formed by the ablation of hot atoms, ions, and clusters from the bulk HEA and their mixing with the liquid's vapor. The plume then cools down, and the ablated species condense into nuclei. The continuous growth of the nuclei is eventually quenched, releasing nanoparticles to the liquid during the collapse of the cavitation bubble. Preparation of the bulk HEA target with the same composition as the HEA nanoparticles of interest is the important step to successfully synthesize the desirable HEA nanoparticles using the laser ablation method. Therefore, the composition space of HEA nanoparticles is limited by the bulk HEAs that can be readily prepared. The synthesis is not sensitive to the pulse duration of the pulsed laser, but the power density is a critical parameter to enable the successful ablation of metals. For example, Waag and co-workers synthesized CoCrFeMnNi HEA nanoparticles in ethanol using picosecond-pulsed laser ablation.[51] Barbero and co-workers used a KrF excimer laser with a pulse duration of 25 ns to synthesize CoNiPtAuCu HEA nanoparticles in a vacuum chamber.[52] Laser ablation has been used to synthesize various HEA nanoparticles in different environments because of the relatively simple setup.[53-59]

In summary, a magnetron co-sputtering system can host multiple metal targets and allow independent control over the vaporization rate of each element, offering the promise in high-throughput screening of HEA nanoparticles with varying compositions and exploration of their properties. The high vacuum requirement for operation limits the magnetron sputtering method in large-scale synthesis. A conventional direct current (DC) arc discharge system generates high-temperature plasma at ambient pressure to vaporize metals, and the gaseous metal atoms are homogeneously mixed in the gas phase, followed by condensation into HEA nanoparticles on a cold collector substrate. The ambient-pressure operation is favorable for scalable synthesis. Although the metal powders of different elements are not necessarily to be alloyed first, they must be carefully mixed and compressed to form the only metal target cathode by considering the different boiling points of different elements that determine their vapor pressures upon arc discharge. The oscillatory (equivalent to AC) spark discharge between two cylindrical electrodes (i.e., one with wire shape and the other with tube shape), which are pre-alloyed metals rather than simply mixed metal powders of different elements, enables the "sparking mashup" method that is efficient to bombard metal atoms from both electrodes and quickly mix them in the electrode gap.

The following nucleation and condensation produce high-concentration HEA nanoparticles in the high-rate gas flow. The directional aerosol flow facilitates the collection of nanoparticles and even additive manufacturing downstream, benefiting large-scale synthesis. The laser ablation synthesis requires HEA metal targets with the same compositions as the synthesized nanoparticles, which can be carried out in gas or liquid phases. The synthesis in a liquid phase can produce colloidal HEA nanoparticles dispersed in the liquid in the presence of capping agents.

5. Burst Reduction

Chemical reduction of metal precursors containing various metal elements is a straightforward strategy to synthesize metal nanoparticles of appropriate compositions by carefully controlling the reaction conditions that determine the reduction reaction and nanoparticle growth kinetics. Simultaneously reducing all metal precursors in a reaction system at comparable reaction rates is crucial to homogeneously mixing the resulting metal atoms, followed by quick nucleation and growth into solid-solution HEA nanoparticles. The sequential reduction of different metal precursors may lead to stepwise nucleation and growth of different metals, forming nanoparticles with compositional segregation. Burst reduction of metal precursors with strong-enough reducing agents, which can level up the reduction rate of different precursors, represents a powerful approach to quickly produce and precipitate metal atoms with ratios defined by the precursor concentrations. The burst production of metal atoms of different elements elevates the supersaturation of all elements within a very short time to trigger the spontaneous homogeneous nucleation, forming nuclei condensed from metal atoms of all elements. The following growth of nanoparticles will simultaneously condense the available metal atoms of all elements to form HEA nanoparticles with homogeneous composition distributions. Figure 7 summarizes the typical methods of promoting burst reduction using various strong reducing species: i) commercially available reducing agents, ii) plasma intermediates, iii) surface spillover hydrogen, and iv) electrons from electrochemical shock.

Hydrides and borohydrides have been widely used as strong reducing agents to synthesize metal nanoparticles for decades. There is no surprise to explore them in synthesizing HEA metal nanoparticles by enabling burst reduction (Figure 7A). For example, the saturated aqueous solution of sodium borohydride ($NaBH_4$) was used to simultaneously reduce $FeSO_4$, $NiSO_4$, $CoSO_4$, $Rh_2(SO_4)_3$, and H_2PtCl_6 dissolved in 2 mM H_2SO_4 aqueous solution containing Ketjen® carbon powders. The product was separated from the solution via centrifugation, followed by washing

with Ar-saturated water/ethanol solution and drying at 70 °C in a glovebox filled with Ar, preventing the potential oxidation of the reduced metals. The dried product was then swiftly transferred to a tube furnace with a gas flow of H_2/Ar and annealed at 350 °C for 3 h, forming ultrasmall NiCoFePtRh HEA nanoparticles.[60] The composition of HEA nanoparticles and the loading of nanoparticles in the composite product could be easily tuned by adjusting the concentrations of metal precursors. HEA nanoparticles of $Fe_{12}Ni_{23}Cr_{10}Co_{55-x}Mn_x$ with tunable Co/Mn ratios were also synthesized using $NaBH_4$ as a reducing agent and carbon nanotubes as support substrates.[16] The FeNiCrCoMn/C composites were annealed at 900 °C in a reducing atmosphere to form a bifunctional oxygen catalyst for rechargeable zinc-air batteries. Singh and Srivastava applied lithium triethyl borohydride ($LiEt_3BH$, or superhydride) to reduce metal chlorides (i.e., $CrCl_2$, $CoCl_2$, $FeCl_2$, $NiCl_2$, and $CuCl_2$) in benzyl ether at the boiling temperature to synthesize NiFeCrCuCo HEA nanoparticles.[61] An argon atmosphere was maintained throughout the entire synthesis to prevent possible oxidation of the synthesized nanoparticles, which were stabilized by adding oleic acid and oleylamine. When metal precursors cannot dissolve in a solvent to mix homogeneously, molten salt can be used to liquify the metal precursors, forming a homogeneous mixture. For instance, precursor metal oxides could mix in molten LiCl at 600-700 °C or molten LiCl-$CaCl_2$ at 500-550 °C. Calcium hydride (CaH_2) was used as reducing agent to reduce oxides of a group metals including Al, Co, Cr, Fe, Ni, and V, which was prepared from their corresponding nitrate salts by following the citric acid method.[62] In a typical synthesis, the metal oxides were mixed with the molten salt and CaH_2 powders in a mortar, followed by being heated to the molten temperature in a stainless-steel reactor filled with an inert atmosphere (e.g., N_2 or Ar). The reduced product was then crushed in a mortar and washed with 0.1 M NH_4Cl aqueous solution and distilled water to remove the molten salt and CaH_2, leaving the synthesized AlCoCrFeNiV HEA nanoparticles. Reduction at a higher temperature of 700 °C led to a fcc structure in the HEA nanoparticles, while reduction at a lower temperature of 550 °C resulted in a bcc structure.

Alkaline metals represent another class of strong reducing agent because of their low reduction potentials (e.g., $E^0_{\mathrm{Na}^+/\mathrm{Na}}$ = -2.713 V vs. standard hydrogen electrode or SHE). Zhang and co-workers used lithium naphthalene (LiNaph), which was prepared by dissolving lithium and naphthalene in tetrahydrofuran (THF) at room temperature in an Ar-filled glovebox, as a reducing agent to reduce a group of metal acetylacetonates.[63] Adding an appropriate amount of dark-green

LiNaph solution to a THF solution containing platinum acetylacetonate [$Pt(acac)_2$], $Co(acac)_2$, $Cu(acac)_2$, $Ni(acac)_2$, and $Fe(acac)_3$ at 62 ^oC (right below the boiling point of THF, 66 ^oC) resulted in the formation of black colloidal nanoparticles containing all five metal elements. Thermally annealing the black product at an appropriate temperature (e.g., 600 ^oC) improved its crystallinity, transforming it into PtFeCoNiCu HEA nanoparticles. When the LiNaph solution contained carbon nanotubes, the synthesis led to the formation of HEA nanoparticles loaded on the carbon nanotubes, which were used as high-performance catalysts for aqueous-phase hydrogenation of maleic anhydride to succinic acid. Chen et al. reported a shear-assisted liquid K-Na droplet surface reduction of metal precursors at room temperature to synthesize HEA nanoparticles.[64] In a typical synthesis of CoFeNiPtTa HEA nanoparticles loaded on carbon black support (Vulcan XC72), the corresponding metal salts, including $Co(acac)_3$, $Fe(acac)_3$, $Ni(acac)_2$, $TaCl_5$, and H_2PtCl_6 and the carbon black were first dispersed in dimethoxyethane (DME) under sonication. After degassing with argon, the dispersion was quickly sheared, and the liquid K-Na (wt % = 1:3) alloy was added to the dispersion to drive the reduction of the metal salts under the protection of argon, forming HEA nanoparticles with sub-2 nm sizes on carbon. The excess K-Na liquid alloy was removed by centrifuging the product with ethanol. When the precursors are composed of only noble metal salts that usually exhibit high reduction potentials, they can be quickly reduced even with a mild reducing agent. For example, Mints and co-workers explored the use of alkaline methanol as a reducing agent to synthesize PtRuPdRhAu HEA nanoparticles with tunable compositions and without surfactant.[65] In a typical synthesis, solid powders of H_2PtCl_6, $HAuCl_3$, $RuCl_3$, $PdCl_2$, and $RhCl_3$ were first dissolved in methanol. An appropriate amount of the precursor solution was then added to a methanolic solution of NaOH containing dispersed high-surface-area carbon support under continuous stirring. The reaction proceeded at room temperature, forming HEA nanoparticles on the carbon support. The carbon support provided high-density active sites for heterogeneous nucleation of HEA nanoparticles, preventing them from growing into large particles. PtRuPdRhAu HEA nanoparticles of 68 different compositions were synthesized to screen the high-performance catalyst for electrochemical oxidation of H_2/CO using Bayesian optimization as guidance.

Electrical discharge in a gas atmosphere generates high-energy plasma, producing many highly reactive intermediate species, including reducing agents. For example, the plasma generated in a H_2/Ar gas contains argon ions (Ar^+), hydrogen radicals ($H^•$), and electrons ($e^–$), in which $H^•$ and

e^- are strong reducing agents. Lee and co-workers blew the atmospheric pressure H_2/Ar plasma into an ionic liquid of [Bmim][Tf_2N] containing a group of metal precursors, i.e., H_2IrCl_6, $Pd(NO_3)_2$, H_2PtCl_6, $Rh(NO_3)_3$, and $RuCl_3$, leading to the synthesis of IrPdPtRhRu HEA nanoparticles (Figure 7B).[66] The HEA nanoparticles adopted the fcc crystalline phase and exhibited a work function of 4.63 eV determined by ultraviolet photoelectron spectroscopy. The valence band emission revealed the hybridization of the metal orbitals in the HEA nanoparticles. This plasma ionic liquid reduction strategy is different from the plasma-enabled vaporization of metals discussed in **Section 4**, where the high temperature of the plasma vaporizes the metal targets made of the elements present in the HEA nanoparticles or the high-energy plasma species bombard the metal targets to atomize metal elements. Wu and co-workers used hydrogen cold plasma (low temperature) generated in a dielectric barrier discharge reactor to simultaneously reduce well-mixed metal chlorides (powder) into HEA nanoparticles.[67] The hydrogen cold plasma consists of energetically active species, including hydrogen anions (H^-), $H^\bullet$, and excited hydrogen molecules (H_2*), which possess strong reducing power with an order of $H^- > H^\bullet > H_2$*. For instance, H^- has a standard reduction potential of –2.3 V (vs. SHE), which is low enough to simultaneously reduce metal ions of many elements into alloys. In a synthesis of PtCrTaVFeAl HEA nanoparticles, the appropriate amounts of H_2PtCl_4, $CrCl_3{\cdot}6H_2O$, $TaCl_5$, VCl_2, $FeCl_3{\cdot}4H_2O$, and $AlCl_3$ powders were mixed in a mortar using a pressed pestle. Before loaded into the reactor, the mixed powder was transferred to a vacuum oven to remove possible moisture. The reactor was purged with Ar gas to remove air and moisture and then H_2 to eliminate oxygen-containing species. After purging, the metal chloride powders were treated with the hydrogen cold plasma at atmospheric pressure, enabling the reduction of metal ions to form HEA nanoparticles. From the thermodynamic point of view, the low standard reduction potential of H^- represents the driving force for the reduction of metal ions. From the kinetic point of view, the high reducing capability of the hydrogen plasma and its near-zero activation time enable the metal ions to be reduced to zero-valence metal atoms instantly and simultaneously. Therefore, abundant metal atoms can be produced in close proximity within a very short time, leading to a burst nucleation followed by random atom deposition of different metal elements. The significantly low reduction potentials of H^- and $H^\bullet$ make the reduction of metal precursors thermodynamically favorable and kinetically fast, leading to the formation of HEA nanoparticles. Carbon support cannot be used in the synthesis to avoid electrical arcs. Instead, nonconductive supporting materials such as ceramic oxides can be used to prevent

the HEA nanoparticles from agglomeration during synthesis. Both examples highlight that converting hydrogen molecules (H_2) to H^- and $H^\bullet$ in a high-energy plasma dramatically increases their reducing power to enable the simultaneous burst reduction of different metal ions.

Hydrogen spillover is a phenomenon capable of dissociating H_2 to adsorbed hydrogen atoms (H*) on the surface of an appropriate reducible transition metal oxide followed by disproportionation into protons and electrons, improving the reducing power. This process involves surface migration of H*, generated from the dissociation of H_2, driven by a concentration gradient. It happens to follow several sequential steps: (i) the dissociative chemisorption of H_2 upon interaction with a noble metal, (ii) the formation of protons (H^+) and e^- from H* atoms at the metal/oxide interface, and (iii) the diffusion of these protons to lattice O^{2-} anions to form O-H and H-O-H bonds and the simultaneous partial reduction of the metal cations in the oxide by the electrons. Therefore, H* atoms migrate to adjacent H-poor reducible metal oxide surfaces, which cannot dissociate H_2, via the coupled proton/electron transfer in the hydrogen spillover process. In contrast, the hydrogen spillover on non-reducible oxide supports is limited because electrons cannot react with the metal cations to simultaneously transfer protons and electrons on the oxide supports. For example, the experimental data and theoretical calculations have shown that hydrogen spillover on TiO_2 proceeds ten orders of magnitude faster than that on the non-reducible Al_2O_3 and that TiO_2 provides longer migration distances from the noble metal proton sources.[68] Mori and co-workers reported the synthesis of CoNiCuRuPd HEA nanoparticles on TiO_2 support by employing the hydrogen spillover process (Figure 7C).[69] The synthesis started with the impregnation of TiO_2 powder in an aqueous solution containing the corresponding metal salt precursors, i.e., $Co(NO_3)_2$, $Ni(NO_3)_2$, $Cu(NO_3)_2$, $RuCl_3$, and Na_2PdCl_4, at room temperature under stirring for 1 h. The water evaporated under vacuum, loading cationic metal precursors on the TiO_2 surface. The sample was reduced in a H_2 flow at 400 °C to form the HEA nanoparticles. The noble metal Pd is used to achieve the hydrogen spillover effect because of its high activity toward dissociative adsorption of H_2. The high reduction potential of Pd^{2+} ($E^0_{Pd^{2+}/Pd}$ = +0.99 V vs. SHE) allows $PdCl_4^{2-}$ to be reduced by H_2, producing Pd atoms that condense into nuclei. The formation of Pd nuclei facilitates the dissociation of H_2 on the surfaces of these Pd nuclei to form Pd-H intermediates (step 1, Figure 7C). The reduction of Ti^{4+} to Ti^{3+} happens with the transfer of H* atoms from the Pd nuclei at the metal/TiO_2 interfaces (step 2). Meanwhile, the electrons migrate from Ti^{3+} to neighbouring Ti^{4+}, promoting the subsequent transfer of protons to O^{2-} attached to the

adjacent Ti^{4+} (step 3). With the assistance of these fast relay steps, the hydrogen atoms rapidly reach all metal ions by moving over the TiO_2 surface (step 4). The metal precursor ions can all be reduced simultaneously to form the HEA nanoparticles (step 5), along with the regeneration of Ti^{4+}. The hydrogen spillover is promoted with the increase in temperature. The reaction at 200 °C results in nanoparticles dominated by Pd nanocrystals, while solid-solution CoNiCuRuPd HEA nanoparticles are formed at 400 °C.

Electrons provided by the working electrode of an electrochemical cell represent a typical class of reducing agents that can simultaneously reduce varying metal precursors at negative enough potentials. Dick's group developed a generalized strategy to synthesize amorphous HEA (or high-entropy metallic glass) nanostructures relying on the stochastic collision of nanodroplets containing metal precursors onto the biased electrode, during which the metal precursors undergo an electro-shock event to enable simultaneous and quick reduction of all precursors.[70] The water nanodroplets are generated from water-in-oil microemulsion by suspending a small volume (e.g., 30 μL) of aqueous solution of all metal precursors in a much larger volume (e.g., 5 mL) of dichloroethane under high-power ultrasonication. Tetrabutylammonium perchlorate (TBAP) is added to dichloroethane as the non-aqueous supporting electrolyte and charge balance mediator during electrochemical reduction of metal precursors. The volume of each nanodroplet is usually in the range of sub-femtoliter (10^{-15} L). The stochastic collision allows for the isolated delivery of individual nanodroplets containing a specific number of precursor metal cations to a localized nucleation and growth domain on the electrode. The contact between a droplet and the electrode is on the order of ~10 nm in radius, and the electrochemical reduction of metal precursors takes a short time on the order of 100 ms.[71] The number of elements and compositions in the HEA nanostructures are conveniently controlled by tuning the concentrations of precursors in the aqueous solution. Figure 7D highlights the characteristic features of a typical collision of a single nanodroplet filled with an aqueous solution of $CoCl_2$, $CrCl_3$, $MnCl_2$, $NiCl_2$, and VCl_3 (5 mM for each precursor) onto a carbon fiber ultramicroelectrode (UME, with a radius of 4 μm). The collision initiates a sharp rise of the cathodic current, followed by a decay due to the consumption of the metal precursor contained inside the nanodroplet. The width of the cathodic peak indicates that electrochemical reduction completes within ~100 ms (left panel, Figure 7D). Integrating the peak area in the current-time curve gives the amount of charge transferred during the reduction process, Q_{red}. The charge of electrons (Q_{ini}) needed to completely reduce the metal precursors

initially contained in each nanodroplet can be calculated using Faraday's Law (right panel, Figure 7D). When these two values are comparable, the metal precursors are fully reduced to zero-valence metals, giving the higher possibility of forming CoCrMnNiV HEA nanostructures with the desired composition. If $Q_{red} < Q_{ini}$, the metal precursors confined in each nanodroplet are partially reduced, making it challenging to form HEA nanostructures with the expected composition. HEA nanostructures made of other metal combinations, including CoCuCrGdNi, CoCrLaMnNiV, CoCrCuGdMnNiV, and CoCrCuGdInMnNiV were also synthesized using this electro-shock method. Because of the burst reduction of all metal precursors at room temperature, the diffusion of metal atoms of different elements is too slow to reach the appropriate locations for forming crystalline structures. The as-synthesized amorphous HEA nanostructures can be annealed in a reducing atmosphere (e.g., in the presence of H_2) at an appropriate temperature (below melting point) to transform them into a crystalline phase. When annealing is performed in an atmosphere of only Ar without H_2, the non-noble metal HEA nanoparticles could be oxidized. For example, Percival and co-workers used the electrochemical shock strategy to synthesize high-entropy oxide nanoparticles of FeNiCoCrMn as an OER catalyst.[72]

In summary, the strong reducing species, including electrons, hydrogen atoms, hydrogen anions, hydrides, and alkaline metals, possess a high reducing power to simultaneously reduce all metal cations in the precursor solution and powder at a high rate. The fast kinetics of the reduction process represents the key factor to enable the homogeneous mixing of different elements in the synthesized HEA nanoparticles. Although the complete reduction can be achieved quickly, the reported syntheses usually span a much longer time (e.g., hours) under the reaction conditions. The extended time facilitates both Wulff construction and Ostwald ripening to improve the crystallinity and uniformity of the HEA nanoparticles. When the reaction temperature is low, the extended time may not be long enough to purify the crystallinity of the nanoparticles, and thermal annealing at elevated temperatures is necessary to yield crystalline HEA nanoparticles. In general, burst reduction of metal precursor cations results in a fast rate to reach supersaturation of metal atoms, triggering burst nucleation with high concentration/number of nanoparticles. As a result, the final nanoparticles usually exhibit small sizes, which makes characterization and verification of the HEA phase challenging. Figure 8 presents the typical techniques useful for analyzing the HEA characteristics of ultrasmall metal nanoparticles, particularly those lacking well-defined XRD peaks. Figure 8A shows a HAADF-STEM image of the NiCoFePtRh HEA nanoparticles

synthesized from burst reduction of metal precursor cations with saturated $NaBH_4$ solution followed by thermal annealing at 350 °C in a gas flow of H_2/Ar.[60] The HEA nanoparticles are dispersed on carbon support due to the strong metal-support interaction that prevents nanoparticle coarsening at elevated temperatures. The average diameter of these HEA nanoparticles is 1.68 nm, which is too small to produce obvious XRD peaks that can differentiate from the XRD peaks of the carbon support. Electron microscopy with atomic resolution can identify the crystallinity of small nanoparticles. Figure 8B is the high-resolution HAADF-STEM image of an individual HEA nanoparticle with only eight atomic layers with an interlayer spacing of 2.10 Å, corresponding to the (111) planes of a fcc phase. Similar to the characterizations of the forementioned examples, EDS mapping and line scan profiles of HEA nanoparticles can be used to identify the homogeneity of spatial distributions of all elements in individual nanoparticles. Figures 8C and 8D show the EDS mapping images of all five elements in a nanoparticle, revealing their uniform distribution and mixing without compositional segregation. The EDS analysis can also give the atomic ratio of different elements, i.e., Ni/Co/Fe/Pt/Rh of 26.6:25.6:25.1:14.9:7.8 for the HEA nanoparticle shown in Figure 8C. The aberration-corrected HAADF-STEM imaging technique is useful to reveal the atomic structure of the small HEA nanoparticles. Figure 8E is the image of a nanoparticle taken along the [011] zone axis, showing the lattice spacings of 2.10 Å and 1.83 Å attributed to the (111) and (200) planes, respectively. Importantly, the high resolution at the atomic scale allows analyzing the crystalline structure of the nanoparticle through fast Fourier transformation (FFT), giving an FFT pattern shown in the inset of Figure 8E. The pattern matches the simulated diffraction pattern of an ideal HEA nanocrystal along its [011] zone axis of an fcc lattice. X-ray absorption fine structure (XAFS) spectroscopy is a powerful technique to analyze the local environment of atoms in a solid, providing information on the electronic structure of atomic coordination in small HEA nanoparticles. The Rh K-edge of the HEA nanoparticles slightly shifts to the left compared to the reference Rh foil (Figure 8F), and the white line intensity of the Pt L_3-edge shows a minor decrease, indicating electron dislocation from neighbouring atoms to Rh and Pt atoms. In contrast, the K-edges of Ni (Figure 8G), Co, and Fe of the HEA nanoparticles slightly shift to the right compared to their corresponding reference metal foils, indicating that atoms of these three elements donate electrons probably due to their low electronegativity. The small size effect of the HEA nanoparticles is responsible for the intensity fluctuation of pre-edge and main features of the X-ray absorption near edge spectroscopy (XANES) rather than the

oxidation effect. All the white lines are far from their corresponding oxide reference samples, confirming that all the elements in the HEA nanoparticles are in metallic states. The comparison of XANES of all elements indicates the redistribution of valence electrons among different atoms in the HEA nanoparticles, which is confirmed by Bader charge analysis. The drift of electron density can fine-tune the electronic structure of HEA nanoparticles, thus influencing their catalytic activity and selectivity. The extended XAFS (EXAFS) spectroscopy can determine the entire coordination structure of five elements in the HEA nanoparticles. The Fourier transforms (FT) of the EXAFS spectra of all elements do not show the M-O (M = Ni, Co, Fe, Pt, Rh) shell, implying that the as-synthesized HEA nanoparticles are not oxidized. The distance of all the first shells (M-M) is shorter than that of the metals of corresponding single elements. Figure 8H plots the FT curves of the first shell for all five elements. The 3*d* transition metal (i.e., Fe, Co, and Ni) absorbers exhibit almost identical distance and amplitude, indicating that they have an identical local atomic structure and homogeneous distributions in the HEA nanoparticles. The distances for Rh and Pt are slightly longer due to their larger atomic radii. Fitting the FT-EXAFS spectra can provide a quantitative local structure, such as the average coordination number (CN). The fitting results show that the CNs of first shell for all elements are almost the same, with a value of ~8.5. The interatomic distances between Fe, Co, and Ni are identical at 2.50 Å, whereas the interatomic distance between Rh and Pt is about 3.85 Å. The EXAFS quantitative analysis also suggests that the five elements in the nanoparticle form a single-phase HEA structure in the form of a solid solution without compositional segregation.

6. Thermal Shock

Metal precursors, including salts containing metal cations and organometallic compounds, can be decomposed into metals through a self-redox reaction (or disproportionation reaction) at a high enough temperature. A large current flow in a carbon fiber or a carbon sheet can generate Joule heat to increase its temperature over 1500 ^{o}C within a very short time (i.e., several milliseconds with a temperature ramping rate of ~10^5 ^{o}C/s) (Figure 9A). The temperature can be controlled and maintained by tuning the electric power supply. Such a high temperature can convert metal precursors attached to the carbon conductors to liquid metals when the temperature is high enough to decompose the precursors into metals and is above the melting point of these metals. Melting the metals of different elements offers a general and powerful way to homogeneously mix metal

atoms of different elements because of the significantly increased diffusivity of atoms in the liquid phase. The thermal shock duration can be short on tens of milliseconds to completely reduce all metal precursors and melt the resulting metals. The poor thermal conductivity of the surrounding gas-phase atmosphere prevents a significant temperature increase in the gas atmosphere during the short thermal shock period, creating a large temperature gradient between the melted metal droplets and the surrounding atmosphere after turning off the electric power supply. The temperature gradient ensures a flash cooling of the metal droplets to freeze the homogeneously mixed atoms into single-phase HEA solids when the cooling rate is appropriate, as highlighted in the TTT diagram of Figure 1A. Prof. Hu's group delivered a pioneering work in 2018 by applying this thermal shock (also called carbothermal shock when using carbon for Joule heating) strategy to synthesize HEA nanoparticles on carbon supports.[4] In a typical synthesis, a carbon fiber film on a glass slide was used for the electric thermal shock. The carbon film was fabricated from electrospun polyacrylonitrile (PAN) fibers that were carbonized at 800 ^{o}C in argon. The carbonization temperature is important to prepare the carbon film with the appropriate defect concentration and electric conductivity for thermal shock synthesis of HEA nanoparticles. A lower carbonization temperature results in a higher concentration of defects that favor the dispersity of nanoparticles, but the carbon film requires a higher voltage and power to induce thermal shock. A higher carbonization temperature yields highly crystalline carbon fibers (with fewer defects), on which the dispersity of nanoparticles is poor, although thermal shock generation becomes easy. Soaking the carbon film in an aqueous solution of mixed metal salt precursors or drop-casting an ethanol solution onto the carbon film loads the precursors on the surfaces of carbon fibers after evaporation of the solvent. The left panel of Figure 9B shows an SEM image of the carbon fiber loaded with the chloride salts of Pt and Ni, revealing the non-uniform distribution of the precursor salts and the presence of micron-sized salt crystals. As a result, reducing the metal salt crystals cannot produce highly dispersed single-phase HEA nanoparticles. Melting the reduced metals via thermal shock becomes crucial to homogeneously mixing the metals and allowing the metal droplets to migrate quickly and shatter into dispersed HEA nanoparticles. An electrical pulse with a duration of 55 ms was applied to the carbon fibers loaded with precursors in an Ar-filled glovebox, achieving a common temperature of ~1700 ^{o}C with a heating/cooling rate up to ~10^5 ^{o}C/s (Figure 10A, right panel). The thermal shock treatment yielded highly dispersed PtNi nanoparticles with well-mixed Pt and Ni atoms (Figure 9B, right panels). Compared to the

precursor salt crystals, the resulting PtNi alloy nanoparticles exhibit a significantly improved dispersity and uniformity in size while the size becomes much smaller. By loading the corresponding metal salt precursors, single-phase HEA nanoparticles made of more elements were synthesized, including quinary combinations (e.g., PtCoNiFeCu, PtPdCoNiFe, PtPdIrRhRu, PtPdRhRuCe), senary combinations (e.g., PtCoNiFeCuAu), septenary combinations (e.g., PtPdCoNiFeCuAu), and octonary combinations (e.g., PtPdCoNiFeCuAuSn). Despite the high tendency to coarse into large droplets of the melted metals upon thermal shock, the inhomogeneity of surface chemistry of the carbon nanofibers, i.e., metal-nonwettable carbon *versus* metal-affinitive surface-bound oxygen (O^*) residuals, forces the liquid metals to shatter into nanosized droplets that strongly bonded to the surface sites with O^*. The following cooling at an appropriate rate (~10^5 $^oC/s$) solidifies individual liquid droplets containing homogeneously mixed different atoms to form solid-solution HEA nanoparticles with a single crystalline phase. The cooling rate is critical in determining the crystalline phases of the resulting nanoparticles. As shown in Figure 1A, a rapid enough quenching is necessary to retain the high-entropy mixing state of the liquid metals and yield single-phase HEA nanoparticles by avoiding the TTT nose. When the cooling rate drops below 10^3 $^oC/s$, nanoscale phase separation occurs to form heterogeneous phase-segregated nanoparticles made of thermodynamically immiscible metals (Figure 1A, right side). In contrast, metallic glass nanoparticles can be formed by maintaining the amorphous phase of the metal liquid as the cooling rate is superfast (Figure 1A, left side).

Because carbon is a commonly used support material for catalysts and the thermal shock synthesis does not need organic capping agents, the as-synthesized HEA nanoparticles represent a promising class of catalysts with better performance than multi-element metal nanoparticles with compositional segregations. This pioneering work opens a new avenue for developing high-performance catalysts with theoretically infinite opportunities. Xie and co-workers used the thermal shock method to synthesize quinary CoMoFeNiCu HEA nanoparticles in a single solid-solution phase with tunable Co/Mo atomic ratios.[73] The success in robust control of the Co/Mo ratio is essential to fully benefit the high entropy effect for catalysis because of their immiscibility according to the Co-Mo phase diagram. Abdelhafiz and co-workers synthesized nanoparticles of all early transition metals, i.e., FeNiCoCrMnV HEA nanoparticles, on gas diffusion layer electrodes using the carbothermal shock method.[74] The HEA nanoparticles can quickly transform to high-entropy oxide/hydroxide (HEO) nanoparticles upon use in aqueous electrolytes, and the

HEO nanoparticles possess higher catalytic activity and stability for OER than a noble metal oxide IrO_2 catalyst. The tunability in the elemental combination and concentration of each element gives a virtually unlimited compositional space in the synthesized HEA nanoparticles, which offers great promise for catalyst discovery but makes the rational and controllable synthesis of ideal HEA catalysts challenging. Yao and co-workers demonstrated the use of computations, including prescreening of millions of compositions, prediction of alloy formation by density functional theory calculations, and examination of structural stability by a hybrid Monte Carlo and molecular dynamics method, to facilitate selecting the favorable HEA compositions for a target reaction.[75] With the computational strategy, nanoparticles made of $Ru_{0.44}Rh_{0.30}Co_{0.12}Ni_{0.14}$ and $Ru_{0.25}Rh_{0.25}Co_{0.2}Ni_{0.2}Ir_{0.1}$ were identified and synthesized as efficient catalysts for ammonia decomposition.

The compositional space can significantly increase with the number of alloyed elements, but general alloying at the nanoscale remains highly challenging due to immiscibility and susceptible oxidation. High-entropy compositional design (i.e., increase in the number of alloyed elements) is critical to enable the alloying of strongly repelled combinations (e.g., Au-W) and easily oxidized elements, including early transition metals. Incorporating the high-entropy-based strategy into carbothermal shock allows the synthesis of HEA nanoparticles with significantly expanded compositions. Figure 9C provides the principle to guide the transition metal alloying by mixing enthalpy and oxidation potentials.[76] The conventionally easy alloys are found under limited conditions with a mild mixing enthalpy (e.g., $\Delta H_{mix} < 3.57$ kJ/mol) and easily reducible metals (e.g., $\Delta G_{oxidation} > -300$ kJ/mol). The entropy contribution at extremely high temperatures ($-T \times \Delta S_{mix}$) becomes significant enough to influence the Gibbs energy change in the alloying process of a large number of elements, such as the 15-element HEA nanoparticles with AuWCuCoNiPtRuMoPdRhFeCrIrSnMn shown in Figure 9D. The 15-element HEA nanoparticles show the extreme mixing of the early and late transition metals, including the strongly repelling Au and W in a uniform alloy structure. The STEM element maps of individual elements exhibit similar spatial intensity distributions, confirming the homogenous mixing of all elements in single nanoparticles and the solid-solution HEA phase. The limiting enthalpy to alloy Au and W is ~25 kJ/mol, which requires high-temperature synthesis combined with high-entropy-driven mixing to make alloying spontaneous. Therefore, synthesizing the 15-element HEA nanoparticles becomes more feasible than synthesizing binary AuW alloy nanoparticles. In contrast, high-temperature

synthesis could overcome the limiting enthalpy (~10 kJ/mol) for directly alloying Au and Co into binary AuCo alloy nanoparticles. The carbothermal reduction can convert transition elements into metallic nanoparticles, and the high-entropy strategy can stabilize them even for the susceptibly oxidized early transition metals, largely extending the alloy spectrum in transition metals by overcoming the immiscibility and inducing metal reduction. For example, element-specific XAS studies of 5-element (CoNiRuRhIr) and 15-element (AuWCuCoNiPtRuMoPdRhFeCrIrSnMn in Figure 9D) HEA nanoparticles show significant differences in the valence states of the easily oxidized elements. The XANES spectrum of a 3*d* transition metal usually exhibits a small bump (i.e., pre-edge feature) located just before the absorption edge, which corresponds to the metallic character.[77] The Co XANES spectrum of the 5-element HEA nanoparticles shows this feature, matching closely with the metallic Co foil, but that of the 15-element HEA nanoparticles lacks this feature. The difference in Ni XANES spectra is insignificant, but the deviation is still observable. The difference in pre-edge features shows that Co and Ni are less metallic in the 15-element HEA nanoparticles. The change of metallic nature of Co and Ni atoms indicates that the high-entropy effect induces redistribution of electron density to shift electron density from the easily oxidized transition metal atoms to the noble metal atoms, stabilizing the easily oxidized elements and preventing them from being oxidized in the 15-element HEA nanoparticles.

Carbon fibers are crucial to enable the carbothermal shock for high-temperature synthesis of HEA nanoparticles, but carbon has a very high diffusion rate in transition metals, particularly at high temperatures. Dissolving carbon in the high-entropy multi-element metal liquid becomes susceptible to possibly forming metal carbides at the HEA/carbon interface upon cooling. Carbon also possibly stays inside the lattice of HEA nanoparticles as octahedral interstitials. Although the formation of interfacial carbides can help bind the HEA nanoparticles to the carbon fiber surfaces, the contamination of carbon in the HEA nanoparticles may influence their properties. Ahn and co-workers tackled this issue by adding a thin titanium (TiO_2) layer that conformally coats the carbon fiber surfaces to prevent direct contact between metals and carbon.[78] Because of the thin thickness, the TiO_2 coating does not turn off the carbothermal shock function of the carbon fibers for high-temperature synthesis of HEA nanoparticles. Figure 9E highlights the major steps in synthesizing HEA nanoparticles on TiO_2-coated carbon fibers. The carbon fiber yarn is first immersed in an ethanolic solution containing metal oxide precursors, such as titanium(IV) tetra isopropoxide, that are easily hydrolyzed upon exposure to water molecules. After immersion for 1 h, the yarn is

removed from the solution and dried in a convection oven at an appropriate temperature (e.g., 60 ^{o}C) to remove the solvent. The precursor adsorbed on the surface starts hydrolysis in the presence of ambient moisture via a sol-gel reaction to form an amorphous oxide layer on the carbon fiber surfaces. In principle, any type of metal precursor that could be hydrolyzed into oxide with an appropriate process should be feasible for producing an oxide coating. A rapid carbothermal shock can convert the amorphous oxide layer to the crystalline one. In the next step, the oxide-coated carbon fibers are immersed in an ethanolic solution containing a mixture of varying metal precursors to load the metal precursor ions onto the oxide surfaces. The positively charged metal cations (e.g., Ti^{4+} for TiO_2) and the negatively charged oxygen ions on the oxide surface lattices can strongly interact with the metal precursor ions (for example, metal chlorides) via electrostatic attractions, enhancing the loading of metal precursors compared to pure carbon fibers. The following drying and carbothermal shock reduce the metal precursors to form HEA nanoparticles. Since the second thermal shock creates instabilities in the oxide lattice, the HEA nanoparticles could be partially embedded in the oxide layer to form a socketed geometry, which can enhance the stability of the HEA nanoparticles against agglomeration under operation conditions. The STEM image in Figure 9E (the right panel) shows RuRhPdIrPt HEA nanoparticles (with an average size of 2.38 nm) on TiO_2-coated carbon fibers synthesized from thermal shock of the corresponding metal chloride precursors, confirming that the HEA nanoparticles are partially embedded in the TiO_2 layer.

The Joule-heating-induced carbothermal shock requires the carbon fibers to be connected to a high-voltage power source and flow a high current, limiting its ability in mass production and the selection of nanoparticle support. In contrast, these limitations could be eliminated if thermal shock is generated by remotely delivering energy to the nanoparticle support. For example, Qiao and co-workers reported the use of microwave heating to synthesize PtPdFeCoNi HEA nanoparticles on reduced graphene sheets.[79] Figure 9F illustrates the major events involved in microwave synthesis. Reducing graphene oxide film in argon at ~570 K eliminates some functional group defects to increase its thermal conductivity, forming a film labeled as rGO-570. The remaining functional group defects are still sufficient to absorb microwave radiation efficiently. In a typical synthesis, drop-casting an appropriate volume of the aqueous solution containing various metal chloride precursors on the rGO-570 loads the precursors to form a composite film labeled precursors/rGO-570 (Figure 9F-i). It is then dried in ambient conditions at room temperature and then sealed in an

Ar-filled glass bottle. The coloured spheres with smaller sizes bonded to the black rGO network represent the remaining functional group defects (e.g., -OH, -COOH, C-O-C), and the metal salt precursor particles are denoted by the larger coloured spheres. Upon microwave heating in Ar (Figure 9F-ii), the rGO-570 film absorbs microwave radiation through the dipoles of the remaining functional group defects to produce heat. The localized heat at the defects can be conducted quickly to the entire sample because of the high thermal conductivity in rGO-570, resulting in uniform heating of the loaded metal salt precursors. The heating can reach a temperature up to ~1850 K within seconds, which is high enough to decompose the precursors into liquid metals and further reduce the rGO-570. The deeply reduced rGO lacks functional group defects and tends to reflect rather than absorb microwave radiation, leading to the automatic cease of the heating process. The subsequent rapid quenching of rGO solidifies the liquid metals into HEA nanoparticles with a single-phase solid solution (Figure 9F-iii). Other carbon substrates, including one-dimensional (1D) carbon nanotubes and three-dimensional (3D) carbonized wood with substantial functional group defects, are also suitable for synthesizing HEA nanoparticles using microwave heating. In principle, any solids with functional groups that can absorb microwave radiation and have high thermal conductivity can be used as support substrates to synthesize HEA nanoparticles.

Compared to carbothermal shock based on Joule heating, the wireless-type microwave heating method does not need the carbon supports to be connected to the external circuit but can still efficiently deliver energy to the species possessing microwave response with high loss tangent. The example presented in Figure 9F highlights the advantages of microwave-enabled carbothermal shock in synthesizing HEA nanoparticles, including high temperature, uniform temperature distribution, fast heating/cooling rate, and easy operation. Because of the wireless feature, microwave heating can be integrated into the roll-to-roll process for scalable synthesis of HEA nanoparticles (Figure 10A).[79] The concept of Figure 10A can be further developed by integrating a constant high-temperature heating zone and a configuration of continuously feeding metal precursors. Figure 10B presents a setup for the fast-moving bed pyrolysis (FMBP) strategy that is capable of synthesizing ultrasmall and highly dispersed HEA nanoparticles composed of up to 10 immiscible elements through pyrolysis of the mixed metal chloride precursors loaded on granular supports that are not limited to carbon substrates.[80] The FMBP strategy can rapidly heat the metal precursors to 923 K within 5 s, when the propulsion speed of the sample holder is 20 cm/s), once the sample holder is moved into the heating zone. The sample holder shows a negligible impact

on the temperature of the heating zone with a drop of only 3 K. These features of the FMBP strategy allow the simultaneous pyrolysis of the dry metal chloride precursors primarily due to the rapid access to the high temperature (equivalent to thermal shock). The fast pyrolysis results in high supersaturation of metal atoms, triggering the burst nucleation and growth of HEA nanoparticles without phase separation. In contrast, the fixed-bed pyrolysis (FBP) strategy can only synthesize phase-separated alloy nanoparticles because of the sequential pyrolysis of different metal precursors during temperature ramping. The metal precursors in a solution, which have a better mixing than the dry precursors on granular supports, can be transported to a high-temperature heating zone in aerosol droplets with micrometer/submicron sizes.[81] Once the aerosol droplets move into the heating zone, the solvent vaporizes instantaneously and does not influence the decomposition of metal precursors and the formation of HEA nanoparticles. The concentration of precursors in the solution and the volume of the droplets determine the size of the HEA nanoparticles. Figure 10C highlights the "droplet-to-particle" aerosol technique coupled with a high-temperature (~2000 K) micro-channel reactor for continuous synthesis of HEA nanoparticles.[82] The micro-channel reactor is built with carbonized wood that is heated by Joule heating. In a typical synthesis, a collision nebulizer generates an aerosol stream of droplets as small as 1 μm in diameter, which are propelled by Ar carrier gas to fly through the micro-channels of the carbonized wood reactor. Once an electrical current is applied to the reactor, the droplets can be heated to 2000 K almost instantaneously due to their small size and the spatial confinement of the micro-channels. The high temperature decomposes the metal precursors into metals and melts them into homogeneously mixed liquid, which rapidly quenches to form HEA nanoparticles with solid-solution phase once the liquid metal droplets fly out the micro-channels.

In summary, the exceptionally high temperature induced by thermal shock is critical for decomposing (or pyrolyzing) metal precursors into metals and melting these metals into liquid with homogeneous mixing of different elements. Solidifying the well-mixed liquid metals into HEA nanoparticles while maintaining the solid-solution phase requires rapid cooling of the high-temperature metal liquid to avoid phase and composition segregation, particularly for the combinations containing immiscible elements. It is necessary to provide a low-temperature environment after the metal liquid is generated at high temperatures, offering a large temperature gradient to enable rapid quenching at a rate $>10^3$ K/s. The carbothermal shock, including wired Joule heating and wireless microwave heating shown in Figure 9, enables the synthesis of HEA

nanoparticles in a gas atmosphere with low thermal conductivity to prevent its temperature from significantly increasing during the short period of thermal shock. As a result, there is a large temperature gradient between the metal liquid and the surrounding gas atmosphere after thermal shock, enabling rapid cooling of the high-temperature metal liquid. The non-uniform affinity of the supports (e.g., carbon fibers, partially reduced graphene oxide, aluminum oxide, titanium oxide, etc.) and the territory of individual flying solution droplets in the aerosol shown in Figure 10C define the sizes of the resulting HEA nanoparticles, preventing them from unrestricted growth. However, the thermal shock strategy becomes highly challenging to solution-phase synthesis because the metals should be selectively heated to be melted while the solvent remains cold to mimic the conditions created in the carbothermal shock method.

Selectively delivering energy to the interesting species at microscopic regions can be a solution to enable mimicking the thermal shock process in the liquid phase. Figure 11A presents a microwave-enabled flash heating and cooling strategy for synthesizing colloidal metal alloy nanoparticles made of immiscible elements in microemulsion micelle nanoreactors dispersed in liquid solutions.[83] By taking the combination of immiscible Au and Pt as an example, the principle of a typical synthesis is addressed as follows. Two water-in-oil (w/o) microemulsion solutions containing the reducing agent of hydrazine and the metal precursors of $HAuCl_4$ and Na_2PtCl_4 are prepared separately by adding an appropriate volume of the corresponding aqueous solutions to a vigorously stirred oil solution containing cyclohexane, *n*-butanol, and cetyltrimethylammonium bromide (CTAB). The microemulsion solution containing hydrazine is denoted as solution **I**, which is stored at room temperature. The microemulsion solution containing metal precursors is denoted as solution **II**, which is stored in a freezer set at –20 ^{o}C for 4 h to form a wax-like solution. In a 10-mL microwave tube reactor, 2 mL of solution **II** and 2 mL of solution **I** are carefully added in a sequential order to keep these two solutions well separated (Figure 11A-a). When a high-power microwave pulse is applied to the microemulsion solutions, the metal precursor ions, hydrazine molecules, water molecules, and *n*-butanol inside the micelles can absorb the microwave energy to increase the temperature of the in-micelle solutions, driving the quick fusion of the two types of micelles to form new micelles containing the well-mixed hydrazine and metal ions (Figure 11A-b. Mixing metal precursor ions and the strong reducing agent (i.e., hydrazine) leads to a quick reduction of the metal precursors into Pt and Au. The fast reduction kinetics at elevated temperatures may help mix the Pt and Au atoms to overcome their thermodynamic immiscibility.

In addition, the nanosized metallic Pt and Au become more efficient in absorbing microwave radiation to rapidly heat them to an extremely high temperature, which could melt them to enable homogenous mixing of Pt and Au atoms (Figure 11A-c). Because of the high efficiency in localized heating, transforming the metal precursors to the melted PtAu in micelles takes only several seconds upon exposure to high-power microwave radiation. In contrast, the oil-phase cyclohexane, representing the most volume of the reaction system, barely absorbs microwave radiation and remains at a low temperature when turning off the microwave. The temperature of the micelle walls, which is mainly determined by the surrounding oil phase, is also low. The large temperature gradient between the melt PtAu and the micelle walls rapidly quenches the melt PtAu. The following solidification yields solid-solution PtAu alloy nanoparticles dispersed on the micelle walls (Figure 11A-d). Mixing additional metal precursors that can be reduced by hydrazine to the microemulsion solution **II** allows the synthesis of solid-solution alloy nanoparticles made of more elements, such as ternary combinations (PtAuPd, PtAuCu) and quaternary combination (PtAuPdCu).[84]

In addition to microwave radiation that can induce localized heating, ultrasound radiation can generate extremely high temperatures in localized microscopic regions at transient timescales due to the associated acoustic cavitation phenomenon. Acoustic cavitation involves the formation, growth, and implosive collapse of microscopic bubbles in a liquid. The bubble collapse generates a localized pressure of up to 2000 atm and a temperature of ~5000 ^{o}C at a transient timescale of nanoseconds (ns) or shorter. The burst release of massive energy at localized microscopic regions is expected to favor the rapid reduction of metal precursors and rapid mixing of the resulting metal atoms into entropy-maximizing states. Liu and co-workers reported the use of ultrasonication to synthesize PtAuPdRhRu HEA nanoparticles from a solution of H_2PtCl_6, $HAuCl_4$, K_2PdCl_4, $RhCl_3$, and $RuCl_3$ dissolved in ethylene glycol, in which an appropriate amount of X-72 carbon was dispersed to serve as support for stabilizing the resulting nanoparticles (Figure 11B).[85] In a typical synthesis, a cylindrical tip of an ultrasonication processor is introduced into the dispersion containing metal precursors and carbon support to deliver ultrasound radiation of 750 watts and 20 kHz for 10 min at room temperature. The as-synthesized HEA nanoparticles with sizes of ~3 nm exhibit a primary fcc phase and a secondary fcc phase as minor constituents. The appearance of such two-phase microstructures could be ascribed to the short timespans of localized high temperatures generated from acoustic cavitation, which might be too short to allow the reduced

metal atoms to mix uniformly before the low-viscosity solution shattered and agitated at the microscopic regions. Further annealing at 700 °C for an extended time (e.g., 2h) transforms the minor secondary phase to the primary fcc phase, resulting in the single-phase PtAuPdRhRu HEA nanoparticles dispersed on carbon support. Replacing ethylene glycol with high-viscosity alcoholic ionic liquid [e.g., N-(2-hydroxyethyl)-N-methylmorpholinium bis(trifluoromethyl sulfonyl) imide] allows to directly synthesize single-phase PtAuPdRhRu HEA nanoparticles on carbon support using ultrasonication.[86] The high viscosity of ionic liquid might confine the reduced metal atoms in the microscopic regions around the bubbles, allowing them to mix well before they cool down to solidify.

In summary, microwave radiation and ultrasound acoustic cavitation have been demonstrated to generate localized high temperatures in the liquid phase and produce multi-principal metal alloy nanoparticles, including the combinations of immiscible elements. The principles of the thermal shock strategy developed for the solid-phase synthesis are feasible to explain the results observed in the liquid-phase synthesis, but the details of time-dependent phase transitions at the microscopic level are still lacking. Developing techniques that allow probing the kinetics of reactions and transitions at microscopic levels will be useful to help better understand the mechanisms of forming HEA nanoparticles.

7. Solvothermal Reduction and Annealing

The microwave and ultrasonication strategies discussed in the previous section show some promise in synthesizing HEA nanoparticles made of noble metals in the liquid phase. The expansion to compositions including non-noble transition metals and *p*-block metals has not been demonstrated yet, and the low popularity of these strategies in wet-chemistry colloidal synthesis is another barrier to attracting more efforts. In contrast, conventional wet-chemistry colloidal synthesis relying on a solvothermal strategy is being adopted to synthesize HEA nanoparticles by taking advantage of the long-time understanding of controlled nucleation and growth of colloidal nanoparticles. Solvothermal synthesis is usually carried out at mild temperatures of <500 °C, where solvent carbonization should be avoided. A pressurized atmosphere is automatically generated above the reaction solution in a sealed reactor (e.g., autoclave) when the temperature exceeds the solvent's boiling point. Iversen group reported a general solvothermal autoclave synthesis of single-phase PtPdIrRhRu HEA nanoparticles by reducing the corresponding metal acetylacetonate

precursors dissolved in a solvent of mixed acetone and ethanol at 200 °C for 24 hours.[87] Alloy nanoparticles made of binary, ternary, and quaternary combinations of these five noble metal elements were also synthesized using the solvothermal method at 200 °C for 4-24 hours. The substantially longer time than the thermal shock strategy is ascribed to the fact that the reduction of metal precursors at the mild temperature needs more time to complete, and the compositional inhomogeneity originated from the sequential reduction of metal precursors takes time to allow sufficient atomic diffusion into single-phase HEA nanoparticles. In-situ synchrotron XRD can be used to follow the evolution of the crystalline phase during the solvothermal process of synthesizing nanoparticles made of different compositions.[88] Rietveld refinement analysis of the time-dependent XRD patterns during the synthesis of single-phase PtPdIrRhRu HEA nanoparticles shows an abrupt increase in scale factor and a simultaneous decrease in the fcc lattice constant from ~3.96 Å to 3.84 Å. The lattice constant stabilizes after 10 min, suggesting that the composition of the growing nanocrystallites does not change and all the five elements precipitate simultaneously at rates with constant ratios. The decrease of lattice constant at the initial stage indicates the overrepresentation of the metals with larger unit cells (e.g., Pd, Pt), which are preferably reduced and nucleate into nanocrystallites upon the start of the reaction. The in-situ XRD studies on the synthesis of nanoparticles made of single elements under the same conditions show significant differences in the temperatures for nanoparticle formation, ranging from 150 °C for Pd, to 200 °C for Pt and Ru, to 250 °C for Rh, to 350 °C for Ir. Since Pd has the lowest precipitation temperature, it is reasonable to hypothesize that Pd dominates the initial nucleation during the synthesis at 200 °C. Five elements precipitate after the initial stage, although the precipitation temperatures for Rh and Ir are higher than 200 °C. The lowered precipitation temperature during HEA synthesis indicates that the initially formed Pd-rich nuclei catalyze the co-reduction and co-deposition of all five elements (Figure 12A). The analysis of XRD peaks also reveals that the apparent average crystallite size along the [111] direction increases preferentially with time until ~20 min compared to that perpendicular to the [111] direction, leading to the nanoparticles with slightly elongated shapes. The autocatalytic deposition of all five elements on the growing nanocrystals continues till the complete consumption of precursors. Agglomeration of the HEA nanoparticles happens due to the absence of capping agents that stabilize individual nanoparticles. The autocatalysis of co-precipitating all five elements implies that forming alloy in this solvothermal synthesis is a kinetically driven process governed by reduction rates of individual

precursors rather than the thermodynamically driven process governed by energy gain of mixing. During the extended reaction time, Pd atoms in the initially formed Pd-rich cores could diffuse outward to improve the mixing homogeneity of all five elements.

The composition of PtPdIrRhRu HEA nanoparticles synthesized using the autoclave solvothermal process can be tuned with some flexibility.[89] However, it cannot be freely tuned as those synthesized using the thermal shock strategy. Systematic studies on the products synthesized from varying nominal concentrations of each precursor show that the 5-element system is highly flexible towards Rh concentration to produce single-phase HEA particles. The system is also flexible towards variations in Pt, Ir, and Ru concentrations, but multiple crystalline phases or non-crystalline particles are formed at high concentrations. The Pd content exhibits the least flexibility to synthesize single-phase nanoparticles, and all samples with increased nominal Pd concentration produce multi-phase products with an additional Pd-rich fcc phase. Performing the autoclave solvothermal synthesis in ethylene glycol, a solvent with stronger reducing power than ethanol, allows the incorporation of non-noble metal elements, including Cu, Co, and Ni, to form single-phase 8-element PtPdIrRhRuCuCoNi HEA nanoparticles.[90] The results of solvothermal synthesis indicate that the combination of autocatalysis and the reducing power of solvent (and added reducing agent) could control the reduction rates of all metal precursors to simultaneously precipitate all metals on the growing nanocrystals with homogeneous mixing. However, the space in tuning the number of elements and the concentration of each element in the single-phase HEA nanoparticles is still limited.

Solvothermal synthesis of colloidal nanocrystals can also be performed without using an autoclave but in solvents with high boiling points, which has been extensively developed for decades for synthesizing nanocrystals made of pure constituents and simple alloys. One typical method so-called “hot injection” relies on fast injection of precursors to a high-temperature solution containing a reducing agent and a capping agent under an appropriate atmosphere (e.g., Ar with atmosphere pressure for preventing oxidation).[91, 92] Dey and co-workers explored the capability of “hot injection” method in synthesizing HEA nanoparticles and investigated their formation mechanism.[93] Three groups of metals, including noble metals (Pd, Pt, Rh, Ir), 3*d* transition metals (Fe, Co, Ni), and a *p*-block metal (Sn) were used to study the feasible combinations for single-phase HEA nanoparticles. The metal precursors for these metals included acetylacetonate salts [$Pd(acac)_2$, $Pt(acac)_2$, $Rh(acac)_3$, $Fe(acac)_3$, $Co(acac)_3$, $Ni(acac)_2$] and

chloride salts ($IrCl_4$, $SnCl_2$). Different metal ions of different oxidation states exhibit a broad range of reduction potentials responsible for the sequential reduction of different metal ions and different reduction rates in the presence of a reducing agent, except those used in burst reduction described in **Section 5**. As a result, the resulting products synthesized from multiple metal ions, particularly the combinations of ≥5 elements for HEA, using the hot injection, usually contain a mixture of nanoparticles made of different compositions or nanoparticles with segregated compositional distributions or nanoparticles with compositions significantly different from the nominal concentrations in the precursors. Dey and co-workers revealed that switching the fast injection of precursor solution in typical operations to slow injection of a dilute precursor solution could lead to the synthesis of HEA nanoparticles with homogeneous mixing of different elements and compositions consistent with the nominal concentrations in the precursor solution.[93] In a typical synthesis of NiPdPtRhIr HEA nanoparticles, 4 mL of a precursor solution containing 8.432 μmol of each salt dissolved in oleylamine is added to a mixed solvent containing 10 mL of octadecene and 6 mL of oleylamine, which are degassed and then protected under Ar and heated to 275 °C, over 10 min at an injection rate of 0.4 mL/min. The slow injection of precursor solution lowers the supersaturation of metal atoms, helping minimize the frequency of collisions between atoms of the same elements to avoid the formation of nanoparticles made of pure elements and the compositional segregation with significant domains of single elements. The continuous precipitation rate of metal atoms more likely falls in the diffusion-limited region, allowing the simultaneous deposition of atoms of different elements at ratios consistent with the nominal ratios in the precursor solution. In the combinations of noble metals and 3*d* transition metals, the reactions at the initial stage always form Pd-rich seeds, on which the reduction of different metal ions and precipitation of metal atoms can be catalyzed to allow the simultaneous deposition of all metal atoms to the surfaces of the Pd-rich seeds. As the nanoparticles grow, the ratio of different elements in the nanoparticles becomes closer to the nominal ratio of different ions in the precursor solution. Although no direct evidence is reported in Dey's work to show the existing Pd-rich core in the synthesized HEA nanoparticles, such an autocatalysis mechanism is reasonable to explain all the observed results and consistent with the mechanism of autoclave solvothermal synthesis. With the addition of $SnCl_2$ to the precursor solution, the SnPdPtRhIr and NiSnPdPtIr HEA nanoparticles could be synthesized without observation of the distinct initial step of forming Pd-rich seeds, indicating that the simultaneous reduction and mixing of all metals is

promoted/catalyzed by the presence of Sn. The results in both autoclave solvothermal and hot injection solvothermal synthesis highlight that Pd and Sn catalyze the simultaneous reduction and precipitation of different metal ions to enable homogeneous mixing in the resulting HEA nanoparticles. The phenomenon is not a surprise in the field of electroless plating. The use of stannous chloride ($SnCl_2$) and palladous chloride ($PdCl_2$) solution has been widely adopted as an electroless plating catalyst since reported in 1950 by Bergström.[94, 95] Despite the relatively lower reduction potentials of Sn^{2+}/Sn and Pd^{2+}/Pd than other metals, Pd^{2+} and Sn^{2+} can be more easily reduced to form tiny nuclei less than 1 nm probably due to their low supersaturation for nucleation. These nuclei catalyze the reduction and precipitation of other elements to enable homogenous mixing in the growing nanoparticles. Although Pd-promoted autocatalysis is not mentioned in some work, this mechanism very likely accounts for the success in synthesizing HEA nanoparticles. For instance, Kitagawa's group synthesized HEA nanoparticles of platinum group elements (e.g., 6-element RuRhPdOsIrPt HEA)[96] and noble metal elements (e.g., 8-element RuRhPdAgOsIrPtAu HEA)[97] by adding an aqueous solution of mixed metal precursors into a preheated triethylene glycol solution containing poly(*N*-vinyl-2-pyrrolidone) (PVP) at a temperature of 230 ^{o}C. Triethylene glycol plays the role of both solvent and reducing agent, while PVP serves as a capping agent to prevent the resulting HEA nanoparticles from aggregation.

If the initially formed nuclei (or small seeds) cannot catalyze the simultaneous reduction and precipitation of all elements during the entire growth, yielding single-phase HEA nanoparticles from the solvothermal synthesis becomes challenging. Skrabalak's group has proposed an alternative approach involving the synthesis of core-shell nanoparticles via seed-mediated co-reduction followed by thermal annealing at a relatively high temperature (e.g., 800 ^{o}C) that is below the metal melting point and much lower than the temperatures required for thermal shock synthesis.[98] Figure 12B highlights the major steps of this approach for synthesizing HEA nanoparticles. The synthesis starts with the preparation of monodisperse bimetallic seed nanoparticles via the traditional hot injection method. The element selection of the bimetallic seeds is determined by the characteristics, particularly the reduction potential, of the metal precursor ions for growing the shells. If the reduction potential of a shell metal precursor is higher than that of a seed element, a galvanic replacement reaction could corrode the seed, impairing the seed-mediated co-reduction of all shell elements to form an ideal alloy shell. With the appropriate bimetallic seeds, three shell metal precursor ions are co-reduced in a hot solution containing

octadecene (solvent), 1,2-dodecanediol (reducing agent), and oleylamine (solvent, reducing agent, and capping agent), resulting in the formation of 5-element core-shell nanoparticles with 2-element cores and 3-element shells. Adding the reducing agent of 1,2-dodecanediol helps reduce the shell metal precursor ions, somehow eliminating the possible galvanic replacement reaction. The core-shell nanoparticles are then dispersed on granular supports, which possess an affinity with the nanoparticles to prevent them from sintering and agglomeration during the following annealing at 800 ^{o}C. Since the annealing temperature is below the melting points of the metals, diffusion of atoms of different elements within individual nanoparticles still requires an extended time (e.g., 2 h) to reach a homogeneous mixing, transforming the core-shell nanoparticles to single-phase HEA nanoparticles. For example, the uniform PdCu intermetallic nanoparticles are used as seeds to mediate the co-reduction of Pt, Ni, and Co from precursors of platinum bromide ($PtBr_2$), nickel acetylacetonate [$Ni(acac)_2$], and cobalt(II) acetate [$Co(ac)_2$], forming PdCu@PtNiCo core-shell nanoparticles. It is worth pointing out that the mixing of the two elements in the intermetallic cores is ordered with B2 structure in the fcc lattice, while the mixing of the three elements in the shells is random. The difference in elemental mixing in the cores and shells helps track the evolution of elemental mixing during thermal annealing, which leads to the formation of single-phase HEA nanoparticles with random elemental mixing in the entire nanoparticles.[99] The successful conversion of PdCu B2@PtNiCo core-shell nanoparticles to single-phase PdCuPtNiCo HEA nanoparticles indicates that the thermal annealing is capable of promoting intradiffusion of atoms within individual nanoparticles to form a solid solution regardless of their atomic orders in the initial core-shell nanoparticles. This modular design and synthesis of core-shell nanoparticles could be generalized to integrate 5 (or more) elements in individual nanoparticles, which are transformed to HEA nanoparticles upon thermal annealing. Synthesizing the appropriate core-shell nanoparticles needs to follow the basic principles: (i) incorporating the metal precursors possessing higher reduction potential (E_{red}) in the core, (ii) depositing the metal precursors possessing much lower E_{red} in the shell, and (iii) putting the metals that are adverse to alloy formation or have poor wettability in the core. With these principles in consideration, AuCu@PdPtNi, PdAg@PtNiCu, PdCu@PtNiAg, PdCu@PtNiCo, PdCo@PtNiCu, and Pd_3Sn@PtNiCu core-shell nanoparticles have been synthesized and converted to single-phase HEA nanoparticles after thermal annealing.[98] Intraparticle heterogeneity of compositional distribution exists in some combinations, for example, PdCu@PtNiRh, PdCu@PtNiIr, and PdCu@PtNiRu. Ni atoms distribute uniformly after annealing

these core-shell nanoparticles, but mixing is incomplete among the other elements, as evidenced by distinct PdCu and PtRh, PtIr, or PtRu random-alloy subdomains.[100] These subdomains are distributed heterogeneously and partially preserve the initial core-shell configuration, possibly because the annealing temperature is not high enough.

The successful transformation of core-shell nanoparticles to single-phase HEA ones via thermal annealing implies that thermal treatment at temperatures below the melting points makes it possible to synthesize single-phase HEA nanoparticles from a solid-state precursor mixture in which the precursor ions of different elements are close enough. For example, annealing the polymetallic metal-organic framework (MOF) at 700 ^{o}C for 2 h in an Ar/H_2 atmosphere can produce fcc CoNiCuMnAl HEA nanoparticles encapsulated in ultrathin carbon shells.[101] The polymetallic MOF is synthesized by following several steps: dissolving cobalt(II) acetate [$Co(ac)_2$], nickel acetate [$Ni(ac)_2$], cupric acetate [$Cu(ac)_2$], manganous acetate [$Mn(ac)_2$], aluminum acetate [$Al(ac)_3$] in N,N-dimethylformamide (DMF) under magnetic stirring for 5 min; injecting 1,4-benzene dicarboxylic acid to the metal salt solution under vigorous magnetic stirring for hours at room temperature; and washing the product with DMF and drying it at 60 ^{o}C under vacuum. Yao and co-workers reported that a solid-state precursor containing various metal ions and 2-methylimidazole was pyrolyzed at 1000 ^{o}C under Ar to produce HEA nanoparticles encapsulated in N-doped hollow carbon nanotubes.[102] The solid-state precursor can be synthesized by following several steps: mixing metal salts including $Zn(NO_3)_2$, $FeCl_3$, $CoCl_2$, $NiCl_2$, $MnCl_2$, and $CuCl_2$ thoroughly via grounding in a mortar; mixing the salt mixture with 2-methylimidazole thoroughly; and heating the mixture at 170 ^{o}C for 1 h.

In summary, a conventional solvothermal process in either autoclave reactors or flasks under ambient pressure is capable of synthesizing colloidal HEA nanoparticles despite the limited compositions. The significant differences in the reduction potentials of different metal precursor ions prevent the simultaneous reduction of all ions at the desired rates under the solvothermal conditions, representing the primary challenge to forming HEA nanoparticles. The most successful examples till now are the synthesis of HEA nanoparticles containing Pd. The high reduction potential of palladium ions ($E_{\mathrm{Pd}^{2+}/\mathrm{Pd}}$ = 0.915 vs. SHE) and relatively low supersaturation of Pd atoms for nucleation favor the quick formation of Pd or Pd-rich nuclei from the solution containing multiple metal precursors at the early reaction stage. The Pd-rich nuclei serve as seeds to catalyze the simultaneous reduction of all metal precursor ions diffused to the nuclei's surfaces and

simultaneous precipitation of the resulting metal atoms to grow the nanoparticles, facilitating the formation of HEA nanoparticles with homogeneous mixing of atoms of different elements. The surface autocatalytic process on the growing nanoparticles levels up the reduction rate of all metal precursor ions to enable simultaneous precipitation of metal atoms of all elements on the growing nanoparticles. If the surface autocatalysis cannot level up the reduction rate of all metal precursors, we can supply metal precursor ions slowly, allowing the nanoparticle growth to fall in the diffusion-limited region. Therefore, the precursor supply will determine the precipitation of metal atoms of all elements on the growing nanoparticles, forming HEA nanoparticles made of homogeneously mixed atoms. When the element combinations contain strongly immiscible metals, seed-mediated co-reduction of metal precursor ions can be employed to prepare core-shell nanoparticles, which can be transformed into single-phase HEA nanoparticles upon thermal annealing. The annealing at elevated temperatures in this two-step procedure increases the diffusivity of atoms within individual core-shell nanoparticles to mix atoms of all elements homogeneously for an extended time.

8. Summary and Outlook

The emergence of HEA metal nanoparticles in 2018 has quickly attracted much attention from a broader research community because the synergistic interactions of different atoms (or cocktail high-entropy effects) make the HEA metal nanoparticles exhibit novel properties and applications. In the past five years, most efforts have focused on developing appropriate methods for synthesizing single-phase HEA nanoparticles with desirable compositions and seeking applications in catalysis, energy storage, and photothermal conversion. The syntheses have produced HEA nanoparticles with a broad range of element combinations and up to 21 elements, which are characterized by a suite of techniques, including electron microscopy imaging, XRD, EDS, and XAFS. These techniques provide information about size and morphology (imaging), crystallinity (XRD), element distributions (EDS), and averaged local environment of specific elements (XAFS). A single set of XRD peaks corresponding to a specific lattice (e.g., fcc or bcc) combined with similar EDS mapping profiles for all elements is the common evidence to determine that the synthesized nanoparticles are single-phase HEA nanoparticles. The XRD peaks of HEA nanoparticles are usually broad due to their small size and intrinsic lattice distortion originating from the significant size difference of different elements. The inhomogeneous

crystallite domains within individual nanoparticles cannot generate XRD signals significant enough to be distinguished from the XRD pattern. The high-resolution EDS mapping profiles of individual nanoparticles are signals collected from the two-dimensional (2D) projection, where the different elements along each atomic column cannot be distinguished. The techniques capable of verifying the random solid solution of different elements at a higher resolution, particularly in three-dimensional (3D) space, could help distinguish the surface alloying state from the subsurface alloying state in individual HEA nanoparticles. Such technical development will help us accurately understand the structure-performance relationship in various applications; for example, the surface alloying state plays the determining role in catalysis, while the subsurface alloying state dominates the photothermal conversion efficiency.

The syntheses reported in the examples discussed in previous sections have demonstrated that there are infinite compositions for HEA nanoparticles to be synthesized in principle. In practice, trying all possible compositions to achieve the functionalities and properties of interest is unnecessary. In the work reported by Yao and co-workers,[75] first-principles calculations were used to aid the selection of appropriate compositions for HEA nanoparticles that could serve as stable and efficient catalysts for NH_3 decomposition. Although the synthesized HEA nanoparticles with the computationally predicted compositions exhibit better catalytic performance than the phase-segregated alloy nanoparticles, the potential of HEA nanoparticles may not be fully unlocked until the real HEA nanoparticles with varying compositions are systematically evaluated. The surface alloying state of the as-synthesized HEA nanoparticles is usually different from the subsurface alloying state and the theoretically calculated surface alloy state, which could cause deviations in catalytic performance between the as-synthesized HEA nanoparticle surfaces and the theoretically predicted surfaces. The experimentally measured performance and properties of HEA nanoparticles of different compositions synthesized at different conditions can be integrated into the computation loop to weigh the influence of synthesis conditions on the physical/chemical parameters of HEA nanoparticles, which is not considered in the first-principles computations. For instance, the PdCuPtNiIr HEA nanoparticles with intraparticle heterogeneity synthesized from the thermal annealing of PdCu@PtNiIr core-shell nanoparticles exhibit better performance than commercial Pt.[100] The PdAgSn/PtBi HEA nanoparticles with Pd-enriched core and Pt-enriched shell show excellent electrocatalytic activity and durability for methanol and ethanol oxidation reactions.[103] Machine learning can help digest the synthesis conditions and experimental

measurements to more accurately predict the synthesis of the HEA nanoparticles with the best catalytic performance when working with the first-principles calculations.

Each method reported for synthesizing HEA nanoparticles has its pros and cons. We have analyzed these methods and summarized them into five categories, identifying the generality and shared principles of different methods. The fundamental principles of each categorized strategy provide the reference guide to design the synthesis methods considering the available resources and the desirable properties of the target HEA nanoparticles. Moreover, hybridizing the metal atom generation of one category with atom condensation of another category may lead to a new synthesis method. For example, the high-power pulse laser used for ablation of HEA metal target can be used to reduce metal salts on carbonaceous support under atmospheric conditions, yielding HEA nanoparticles dispersed on the carbon support.[104] When a graphene layer absorbs laser photons, electrons from the valence band are excited to the conduction band to achieve and maintain the population inversion state. Through an Auger-like mechanism, hot electrons gaining enough energy can eject from the graphene to become free electrons. The free electrons represent a class of powerful reducing agents, as discussed in **Section 5,** that can trigger burst reduction of metal precursors. The electron flow can also propel the precursor powder across the reaction container to achieve an even and homogeneous reaction (Figure 13A). Delivering the laser energy packages with a pulse duration of 5 ns and a pulse energy of up to 600 mJ to graphene can generate an apparent plasma plume containing electron jet flow (Figure 13B). The formation of HEA nanoparticles on the graphene support involves several steps (Figure 13C). The photons are absorbed in the graphene and metal ions to generate free electrons and high temperature, triggering the reduction of metal ions and etching of the graphene. The laser-induced plume containing ejected free electrons maintains a reductive atmosphere to prevent oxidation of metal nanoparticles, allowing the synthesis applicable in air. The reduced metal atoms are instantly cooled down after laser irradiation and condense into small HEA nanoparticles on the graphene defect sites. The laser-induced ultrafast reduction and cooling in nanoseconds can synthesize supported HEA nanoparticles made of a broad range of compositions in a scalable manner. Jiang and co-workers showed the synthesis of various HEA nanoparticles with sizes of 1-3 nm and the number of metal elements up to 11 with a yield of up to 7 grams per hour.[104]

The crucial requirement for forming single-phase HEA nanoparticles through bottom-up synthesis is the simultaneous generation of metal atoms of all elements at rates proportional to

their nominal concentrations in the HEA nanoparticles. "Vaporization of metals" controls the generation rate of metal atoms through the bombardment power and the fraction of elements in the metal targets. "Burst reduction" usually reduces all metal precursors quickly to level up the atom generation rate of all elements. "Thermal shock" can also reduce all metal precursors and melt the reduced metals within the short thermal shock period. Therefore, the metal atoms generated via these three strategies can simultaneously precipitate/solidify into solid-solution HEA nanoparticles. In contrast, the simultaneous reduction of metal precursors of different elements in solvothermal synthesis is not guaranteed, as discussed in **Section 7**. Since the solvothermal synthesis of colloidal nanoparticles involves many tunable functions, including both chemical and physical parameters, there is much room to explore for synthesizing HEA nanoparticles despite the challenges. For example, switching "fast injection" in conventional solvothermal synthesis of single-element metal nanoparticles to "slow injection" of diluted precursor solution enables the synthesis of seven colloidal HEA nanoparticles that contain various combinations of noble metals (Pd, Pt, Rh, Ir), 3*d* transition metals (Ni, Fe, Co), and a *p*-block element (Sn).[93] The switching of injection mode significantly changes the reduction kinetics of different precursors in the synthesis systems. Quantitative studies reveal that the slow dropwise injection allows the reduction of different metal precursor ions to reach a steady state, at which the generation rate of atoms of different elements becomes the same if the concentration of each precursor is the same in the precursor solution. Quantitatively knowing the delay times for reaching the steady state makes it possible to predict the structures and spatial compositions of the synthesized nanoparticles. For example, Liu and co-workers reported the synthesis of homogeneous HEA nanoparticles, homogeneous HEA dendrites, and heterogeneous core-shell nanoparticles made of PdPtRhIrRu by tuning the reduction kinetics and the delay time for a steady state.[105] The dendritic HEA nanocrystals with a defect-rich surface show a substantial increase in catalytic performance for hydrogen evolution and oxidation compared to the phase-segregated counterparts. Therefore, synthesizing HEA nanoparticles with well-defined shapes represents a future direction. Although the shaped-controlled synthesis of colloidal metal nanoparticles made of single elements and simple alloys has been extensively studied, synthesizing colloidal HEA nanoparticles with shapes other than spheres is still rare.[106, 107] Once the controllability is achieved, the solvothermal synthesis can be easily scaled up or adopted in the continuous-flow reactors to enable mass production.[108, 109] The availability of high-

quality single-phase HEA nanoparticles with well-defined shapes will provide a class of new materials platform to discover novel properties and explore their applications.

The sluggish diffusion of atoms in HEA solids at low temperatures (e.g., room temperature) helps stabilize the synthesized HEA nanoparticles. However, the diffusion of atoms significantly increases upon the increase of temperature, rearranging the atoms into (locally) ordered structures particularly when the HEA nanoparticles are composed of immiscible elements. In some cases, such a disorder-to-order phase transition in the HEA nanoparticles leads to the formation of intermetallic structures, which is so-called high-entropy intermetallic (HEI). The constituent metal atoms of a HEI nanoparticle are distributed separately to two crystallographically distinct sites determined by the parent intermetallic structure made of two metal elements. Cui and co-workers applied Joule heating to reheat the octonary HEA nanoparticles made of PtPdAuFeCoNiCuSn at ~1100 K for 5 minutes to rearrange the metal atoms into a more thermodynamically stable HEI configuration, followed by rapid cooling to lock the HEI phase.[110] The resulting HEI nanoparticles exhibit an intermetallic structure with two sublattices (A_1B_1), in which the noble metal atoms Pt, Pd, and Au randomly distribute in sublattice A and the non-noble metal atoms Fe, Co, Ni, Cu, and Sn randomly distributed in sublattice B. The HEA-to-HEI phase transition is a thermodynamically process, which can benefit the extended heating period. In contrast, the synthesis of thermodynamically less stable solid-solution HEA nanoparticles through the thermal shock approach in **Section 6** requires a much shorter time (e.g., ~50 ms), highlighting the importance of balancing kinetic and thermodynamic control on determining the phase structure of alloy nanoparticles. The higher thermodynamic stability of a HEI than its counterpart HEA with the same composition makes the synthesis of HEI nanoparticles less dependent on the extreme kinetic controls used in the synthesis of HEA nanoparticles. Therefore, direct synthesis of HEI nanoparticles from the corresponding metal precursors with the appropriate compositions becomes feasible even using the conventional near-equilibrium reaction conditions, such as hydrogen reduction at elevated temperatures and solvothermal reduction for an extended time. For example, Prof. Furukawa's group developed a pore-filling co-impregnation method to synthesize various HEI nanoparticles on granular oxide support.[111-113] An aqueous solution containing all metal precursors is first added dropwise to the oxide powder, followed by ageing at room temperature. The aged mixture is then slowly dried through freeze drying or rotary evaporation, depositing the metal precursors into the pores of the oxide powder. The composite powder is calcinated an

elevated temperature in dry air followed by reduction in H_2 at a higher temperature, resulting in the formation of HEI nanoparticles on the oxide support. By taking PtGe as the intermetallic blueprint with space group of *Pnma* (FeAs-type structure), synthesis using the metal precursor mixture of $Pt(NH_3)_2(NO_3)_2$, $Co(NO_3)_2$, $Cu(NO_3)_2$, $(NH_4)_2GeF_6$, $Ga(NO_3)_3$, and $(NH_4)_2SnCl_6$ leads to the formation of (PtCoCu)(GeGaSn) HEI nanoparticles, in which Pt, Co, and Cu atoms mix randomly in one sublattice and Ge, Ga, and Sn mix randomly in another sublattice.[111] HEI nanoparticles of (NiFeCu)(GaGe) and (PtCoNi)(SnInGa) are also successfully synthesized following the intermetallic structure of NiGa and PtSn, respectively.[112, 113] Chen and co-workers used solvothermal reduction of a metal precursor mixture including $Pt(acac)_2$, $Rh(acac)_3$, $Bi(ac)_3$, $SnCl_2$, and $SbCl_3$ with ascorbic acid in octadecene and oleylamine containing cetyltrimethyl ammonium bromide (CTAB) at 220 ^oC to synthesize (PtRh)(BiSnSb) HEI nanoplates with structure close to PtSn.[114] In a bimetallic intermetallic, each type of atoms occupy one sublattice, in which each atom coordinates only two atoms of the same type. Randomly mixing/replacing the interesting atoms with other metals in a HEI makes it easy to isolate the interesting atoms in the HEI lattice. Therefore, HEI nanoparticles provide a class of single-atom catalysts with high surface density. Despite the relatively lower entropy of a HEI than its counterpart HEA with the same composition, the unique structure (e.g., single atom distribution) and thermal stability of the HEI nanoparticles broaden the materials spectrum of multiple principal metal alloy nanoparticles.

Acknowledgements

Y. Sun thanks the support of the National Science Foundation (NSF) of the United States under the NSF award 1946912.

References

1. B. Cantor, I. T. H. Chang, P. Knight and A. J. B. Vincent, *Materials Science and Engineering: A*, 2004, **375-377**, 213-218.
2. J.-W. Yeh, S.-K. Chen, S.-J. Lin, J.-Y. Gan, T.-S. Chin, T.-T. Shun, C.-H. Tsau and S.-Y. Chang, *Advanced Engineering Materials*, 2004, **6**, 299-303.
3. W. S. Hume-Rothery, R. E.; Haworth, C. W., *The Structure of Metals and Alloys*, Metals & Metallurgy Trust, London, 1969.

4. Y. Yao, Z. Huang, P. Xie, S. D. Lacey, R. J. Jacob, H. Xie, F. Chen, A. Nie, T. Pu, M. Rehwoldt, D. Yu, M. R. Zachariah, C. Wang, R. Shahbazian-Yassar, J. Li and L. Hu, *Science*, 2018, **359**, 1489-1494.
5. K. Y. Tsai, M. H. Tsai and J. W. Yeh, *Acta Materialia*, 2013, **61**, 4887-4897.
6. T. A. A. Batchelor, J. K. Pedersen, S. H. Winther, I. E. Castelli, K. W. Jacobsen and J. Rossmeisl, *Joule*, 2019, **3**, 834-845.
7. T. Löffler, A. Savan, A. Garzón-Manjón, M. Meischein, C. Scheu, A. Ludwig and W. Schuhmann, *ACS Energy Letters*, 2019, **4**, 1206-1214.
8. Y. Sun and S. Dai, *Science Advances*, 2021, **7**, eabg1600.
9. G. M. Tomboc, T. Kwon, J. Joo and K. Lee, *Journal of Materials Chemistry A*, 2020, **8**, 14844-14862.
10. B. Wang, Y. Yao, X. Yu, C. Wang, C. Wu and Z. Zou, *Journal of Materials Chemistry A*, 2021, **9**, 19410-19438.
11. Y. Wang and Y. Wang, *Nano Energy*, 2022, **104**, 107958.
12. Y. Xin, S. Li, Y. Qian, W. Zhu, H. Yuan, P. Jiang, R. Guo and L. Wang, *ACS Catalysis*, 2020, **10**, 11280-11306.
13. H. Xu, Z. Jin, Y. Zhang, X. Lin, G. Xie, X. Liu and H.-J. Qiu, *Chemical Science*, 2023, **14**, 771-790.
14. L. Yu, K. Zeng, C. Li, X. Lin, H. Liu, W. Shi, H.-J. Qiu, Y. Yuan and Y. Yao, *Carbon Energy*, 2022, **4**, 731-761.
15. H. Zheng, G. Luo, A. Zhang, X. Lu and L. He, *ChemCatChem*, 2021, **13**, 806-817.
16. X. Cao, Y. Gao, Z. Wang, H. Zeng, Y. Song, S. Tang, L. Luo and S. Gong, *ACS Applied Materials & Interfaces*, 2023, **15**, 32365-32375.
17. E. Shen, X. Song, Q. Chen, M. Zheng, J. Bian and H. Liu, *ChemElectroChem*, 2021, **8**, 260-269.
18. X. Wang, Q. Dong, H. Qiao, Z. Huang, M. T. Saray, G. Zhong, Z. Lin, M. Cui, A. Brozena, M. Hong, Q. Xia, J. Gao, G. Chen, R. Shahbazian-Yassar, D. Wang and L. Hu, *Advanced Materials*, 2020, **32**, 2002853.
19. Y. Wei, X. Liu, R. Yao, J. Qian, Y. Yin, D. Li and Y. Chen, *Journal of Alloys and Compounds*, 2023, **938**, 168610.

20. X. Xu, Y. Du, C. Wang, Y. Guo, J. Zou, K. Zhou, Z. Zeng, Y. Liu and L. Li, *Journal of Alloys and Compounds*, 2020, **822**, 153642.
21. Y. Ai, M.-Q. He, H. Sun, X. Jia, L. Wu, X. Zhang, H.-b. Sun and Q. Liang, *Advanced Materials*, 2023, **35**, 2302335.
22. Y. Li, Y. Liao, J. Zhang, E. Huang, L. Ji, Z. Zhang, R. Zhao, Z. Zhang, B. Yang, Y. Zhang, B. Xu, G. Qin and X. Zhang, *Angewandte Chemie International Edition*, 2021, **60**, 27113-27118.
23. Y. Li, Y. Ma, Y. Liao, L. Ji, R. Zhao, D. Zhu, X. Hu, G. Qin, H. Rong and X. Zhang, *Advanced Energy Materials*, 2022, **12**, 2203057.
24. Y. Li, L. Yang, Y. Liao, R. Zhao, L. Ji, R. Su, D. Xu and F. Wang, *Advanced Functional Materials*, 2023, **33**, 2302712.
25. Y. Liao, Y. Li, L. Ji, X. Liu, X. Zhao, H. Rong, D. Xu, G. Qin and X. Zhang, *Acta Materialia*, 2022, **240**, 118338.
26. Y. Liao, Y. Li, R. Zhao, J. Zhang, L. Zhao, L. Ji, Z. Zhang, X. Liu, G. Qin and X. Zhang, *National Science Review*, 2022, **9**, nwac041.
27. Y. Zhou, X. Shen, T. Qian, C. Yan and J. Lu, *Nano Research*, 2023, **16**, 7874-7905.
28. Y.-B. Lu, G.-X. Zhang, F.-Y. Yang, M.-Q. Yao, L.-Y. Liu and H. Pang, *Rare Metals*, 2023, **42**, 3212-3245.
29. W. Wan, K. Liang, P. Zhu, P. He and S. Zhang, *Journal of Materials Science & Technology*, 2024, **178**, 226-246.
30. J. Li, Y. Chen, Q. He, X. Xu, H. Wang, C. Jiang, B. Liu, Q. Fang, Y. Liu, Y. Yang, P. K. Liaw and C. T. Liu, *Proceedings of the National Academy of Sciences*, 2022, **119**, e2200607119.
31. N. Kumar, C. S. Tiwary and K. Biswas, *Journal of Materials Science*, 2018, **53**, 13411-13423.
32. N. Kumar and K. Biswas, *Review of Scientific Instruments*, 2015, **86**, 083903.
33. S. Nellaiappan, N. K. Katiyar, R. Kumar, A. Parui, K. D. Malviya, K. G. Pradeep, A. K. Singh, S. Sharma, C. S. Tiwary and K. Biswas, *ACS Catalysis*, 2020, **10**, 3658-3663.
34. L. Sharma, N. K. Katiyar, A. Parui, R. Das, R. Kumar, C. S. Tiwary, A. K. Singh, A. Halder and K. Biswas, *Nano Research*, 2022, **15**, 4799-4806.

35. K. Barai, C. S. Tiwary, P. P. Chattopadhyay and K. Chattopadhyay, *Materials Science and Engineering: A*, 2012, **558**, 52-58.
36. S. Varalakshmi, M. Kamaraj and B. S. Murty, *Journal of Alloys and Compounds*, 2008, **460**, 253-257.
37. Y. Zhang, X. Li, Q. Qin, J. Li, H. Zhao, X. Gao, X. Su and D. Chen, *Materials Science and Technology*, 2021, **37**, 545-551.
38. M. Y. Rekha, N. Mallik and C. Srivastava, *Scientific Reports*, 2018, **8**, 8737.
39. H. Le-The, E. Berenschot, R. M. Tiggelaar, N. R. Tas, A. van den Berg and J. C. T. Eijkel, *Microsystems & Nanoengineering*, 2018, **4**, 4.
40. T. Löffler, H. Meyer, A. Savan, P. Wilde, A. Garzón Manjón, Y.-T. Chen, E. Ventosa, C. Scheu, A. Ludwig and W. Schuhmann, *Advanced Energy Materials*, 2018, **8**, 1802269.
41. D. König, K. Richter, A. Siegel, A.-V. Mudring and A. Ludwig, *Advanced Functional Materials*, 2014, **24**, 2049-2056.
42. H. Meyer, M. Meischein and A. Ludwig, *ACS Combinatorial Science*, 2018, **20**, 243-250.
43. E. Redel, M. Walter, R. Thomann, C. Vollmer, L. Hussein, H. Scherer, M. Krüger and C. Janiak, *Chemistry – A European Journal*, 2009, **15**, 10047-10059.
44. A. Dvurečenskij, A. Cigáň, P. Lobotka, G. Radnóczi, M. Škrátek, J. Benyó, E. Kováčová, M. Majerová and J. Maňka, *Journal of Alloys and Compounds*, 2022, **896**, 163089.
45. X. Zhang, J. Guo, P. Guan, C. Liu, H. Huang, F. Xue, X. Dong, S. J. Pennycook and M. F. Chisholm, *Nature Communications*, 2013, **4**, 1924.
46. A. Mao, H. Xiang, X. Ran, Y. Li, X. Jin, H. Yu and X. Gu, *Journal of Alloys and Compounds*, 2019, **775**, 1177-1183.
47. Y. Li, Y. Liao, L. Ji, C. Hu, Z. Zhang, Z. Zhang, R. Zhao, H. Rong, G. Qin and X. Zhang, *Small*, 2022, **18**, 2107265.
48. J. Feng, D. Chen, P. V. Pikhitsa, Y.-h. Jung, J. Yang and M. Choi, *Matter*, 2020, **3**, 1646-1663.
49. Q. Wu, Z. Wang, F. He, L. Wang, J. Luo, J. Li and J. Wang, *Metallurgical and Materials Transactions A*, 2018, **49**, 4986-4990.
50. K. Suliz, A. Miller, K. Ivanov and A. Pervikov, *Powder Technology*, 2022, **404**, 117491.
51. F. Waag, Y. Li, A. R. Ziefuß, E. Bertin, M. Kamp, V. Duppel, G. Marzun, L. Kienle, S. Barcikowski and B. Gökce, *RSC Advances*, 2019, **9**, 18547-18558.

52. A. Barbero, C. Moreira Da Silva, N. Ortiz Pena, N. Kefane, A. Jaafar, M. Thorey, H. Bouaia, J. Nelayah, G. Wang, H. Amara, C. Ricolleau, V. Huc and D. Alloyeau, *Faraday Discussions*, 2023, **242**, 129-143.
53. A. Abdelhafiz, A. N. M. Tanvir, M. Zeng, B. Wang, Z. Ren, A. R. Harutyunyan, Y. Zhang and J. Li, *Advanced Science*, 2023, **10**, 2300426.
54. S. Bag, A. Baksi, D. Wang, R. Kruk, C. Benel, M. R. Chellali and H. Hahn, *Nanoscale Advances*, 2019, **1**, 4513-4521.
55. H. Jahangiri, Y. Morova, A. Asghari Alamdari, Z. Eroğlu, A. Sennaroğlu, S. Guo, O. Metin and A. Motallebzadeh, *Intermetallics*, 2023, **156**, 107834.
56. J. Johny, Y. Li, M. Kamp, O. Prymak, S.-X. Liang, T. Krekeler, M. Ritter, L. Kienle, C. Rehbock, S. Barcikowski and S. Reichenberger, *Nano Research*, 2022, **15**, 4807-4819.
57. Z. Lin, J. Yue, L. Liang, B. Tang, B. Liu, L. Ren, Y. Li and L. Jiang, *Applied Surface Science*, 2020, **504**, 144461.
58. H. Pérez Blanes, P. Ghiasi, J. Sandkühler, Y. Yesilcicek, S. Pentzien, A. Conradi, C. Prinz, D. Al-Sabbagh, A. F. Thünemann, O. Ozcan and J. Witt, *Journal of Materials Research and Technology*, 2023, **24**, 9434-9440.
59. R. Rawat, B. K. Singh, A. Tiwari, N. Arun, A. P. Pathak, Y. Shadangi, N. K. Mukhopadhyay, S. R. Nelamarri, S. V. Rao and A. Tripathi, *Journal of Alloys and Compounds*, 2022, **927**, 166905.
60. G. Feng, F. Ning, J. Song, H. Shang, K. Zhang, Z. Ding, P. Gao, W. Chu and D. Xia, *Journal of the American Chemical Society*, 2021, **143**, 17117-17127.
61. M. P. Singh and C. Srivastava, *Materials Letters*, 2015, **160**, 419-422.
62. Y. Kobayashi, D. Suzuki, S. Yokoyama and R. Shoji, *International Journal of Hydrogen Energy*, 2022, **47**, 3722-3732.
63. N. Zhang, X. Chen, S. Liu, J. Meng, M. Armbrüster and C. Liang, *ACS Applied Materials & Interfaces*, 2023, **15**, 23276-23285.
64. H. Chen, C. Guan and H. Feng, *ACS Applied Nano Materials*, 2022, **5**, 9810-9817.
65. V. A. Mints, J. K. Pedersen, A. Bagger, J. Quinson, A. S. Anker, K. M. Ø. Jensen, J. Rossmeisl and M. Arenz, *ACS Catalysis*, 2022, **12**, 11263-11271.
66. G. Lee, N.-A. Nguyen, V.-T. Nguyen, L. L. Larina, E. Chuluunbat, E. Park, J. Kim, H.-S. Choi and M. Keidar, *Journal of Solid State Chemistry*, 2022, **314**, 123388.

67. D. Wu, L. Yao, M. Ricci, J. Li, R. Xie and Z. Peng, *Chemistry of Materials*, 2022, **34**, 266-272.
68. W. Karim, C. Spreafico, A. Kleibert, J. Gobrecht, J. VandeVondele, Y. Ekinci and J. A. van Bokhoven, *Nature*, 2017, **541**, 68-71.
69. K. Mori, N. Hashimoto, N. Kamiuchi, H. Yoshida, H. Kobayashi and H. Yamashita, *Nature Communications*, 2021, **12**, 3884.
70. M. W. Glasscott, A. D. Pendergast, S. Goines, A. R. Bishop, A. T. Hoang, C. Renault and J. E. Dick, *Nature Communications*, 2019, **10**, 2650.
71. J. Reyes-Morales and J. E. Dick, *Accounts of Chemical Research*, 2023, **56**, 1178-1189.
72. S. J. Percival, P. Lu, D. R. Lowry and T. M. Nenoff, *Langmuir*, 2022, **38**, 1923-1928.
73. P. Xie, Y. Yao, Z. Huang, Z. Liu, J. Zhang, T. Li, G. Wang, R. Shahbazian-Yassar, L. Hu and C. Wang, *Nature Communications*, 2019, **10**, 4011.
74. A. Abdelhafiz, B. Wang, A. R. Harutyunyan and J. Li, *Advanced Energy Materials*, 2022, **12**, 2200742.
75. Y. Yao, Z. Liu, P. Xie, Z. Huang, T. Li, D. Morris, Z. Finfrock, J. Zhou, M. Jiao, J. Gao, Y. Mao, J. Miao, P. Zhang, R. Shahbazian-Yassar, C. Wang, G. Wang and L. Hu, *Science Advances*, 2020, **6**, eaaz0510.
76. Y. Yao, Z. Huang, L. A. Hughes, J. Gao, T. Li, D. Morris, S. E. Zeltmann, B. H. Savitzky, C. Ophus, Y. Z. Finfrock, Q. Dong, M. Jiao, Y. Mao, M. Chi, P. Zhang, J. Li, A. M. Minor, R. Shahbazian-Yassar and L. Hu, *Matter*, 2021, **4**, 2340-2353.
77. D. Morris, Y. Yao, Y. Z. Finfrock, Z. Huang, R. Shahbazian-Yassar, L. Hu and P. Zhang, *Cell Reports Physical Science*, 2021, **2**, 100641.
78. J. Ahn, S. Park, D. Oh, Y. Lim, J. S. Nam, J. Kim, W. Jung and I.-D. Kim, *ACS Nano*, 2023, **17**, 12188-12199.
79. H. Qiao, M. T. Saray, X. Wang, S. Xu, G. Chen, Z. Huang, C. Chen, G. Zhong, Q. Dong, M. Hong, H. Xie, R. Shahbazian-Yassar and L. Hu, *ACS Nano*, 2021, **15**, 14928-14937.
80. S. Gao, S. Hao, Z. Huang, Y. Yuan, S. Han, L. Lei, X. Zhang, R. Shahbazian-Yassar and J. Lu, *Nature Communications*, 2020, **11**, 2016.
81. Y. Yang, B. Song, X. Ke, F. Xu, K. N. Bozhilov, L. Hu, R. Shahbazian-Yassar and M. R. Zachariah, *Langmuir*, 2020, **36**, 1985-1992.

82. X. Wang, Z. Huang, Y. Yao, H. Qiao, G. Zhong, Y. Pei, C. Zheng, D. Kline, Q. Xia, Z. Lin, J. Dai, M. R. Zachariah, B. Yang, R. Shahbazian-Yassar and L. Hu, *Materials Today*, 2020, **35**, 106-114.
83. D. Zhang, C. Chen, X. Wang, G. Guo and Y. Sun, *Particle & Particle Systems Characterization*, 2018, **35**, 1700413.
84. S. Wu, Y. Liu, Y. Ren, Q. Wei and Y. Sun, *Nano Research*, 2022, **15**, 4886-4892.
85. M. Liu, Z. Zhang, F. Okejiri, S. Yang, S. Zhou and S. Dai, *Advanced Materials Interfaces*, 2019, **6**, 1900015.
86. F. Okejiri, Z. Yang, H. Chen, C.-L. Do-Thanh, T. Wang, S. Yang and S. Dai, *Nano Research*, 2022, **15**, 4792-4798.
87. M. Bondesgaard, N. L. N. Broge, A. Mamakhel, M. Bremholm and B. B. Iversen, *Advanced Functional Materials*, 2019, **29**, 1905933.
88. N. L. N. Broge, M. Bondesgaard, F. Søndergaard-Pedersen, M. Roelsgaard and B. B. Iversen, *Angewandte Chemie International Edition*, 2020, **59**, 21920-21924.
89. A. D. Bertelsen, A. R. Hansen, N. L. N. Broge, A. Mamakhel, M. Bondesgaard and B. B. Iversen, *Chemical Communications*, 2022, **58**, 12672-12675.
90. N. L. N. Broge, A. D. Bertelsen, F. Søndergaard-Pedersen and B. B. Iversen, *Chemistry of Materials*, 2023, **35**, 144-153.
91. S. Peng, J. M. McMahon, G. C. Schatz, S. K. Gray and Y. G. Sun, *Proceedings Of the National Academy of Sciences of the United States of America*, 2010, **107**, 14530-14534.
92. S. Peng, C. H. Lei, Y. Ren, R. E. Cook and Y. G. Sun, *Angewandte Chemie International Edition*, 2011, **50**, 3158-3163.
93. G. R. Dey, C. R. McCormick, S. S. Soliman, A. J. Darling and R. E. Schaak, *ACS Nano*, 2023, **17**, 5943-5955.
94. E. A. Bergstrom, *Surface metallizaing* method, US Patent 2702235, 1950.
95. X. Wei and D. K. Roper, *Journal of The Electrochemical Society*, 2014, **161**, D235.
96. D. Wu, K. Kusada, T. Yamamoto, T. Toriyama, S. Matsumura, S. Kawaguchi, Y. Kubota and H. Kitagawa, *Journal of the American Chemical Society*, 2020, **142**, 13833-13838.
97. D. Wu, K. Kusada, Y. Nanba, M. Koyama, T. Yamamoto, T. Toriyama, S. Matsumura, O. Seo, I. Gueye, J. Kim, L. S. Rosantha Kumara, O. Sakata, S. Kawaguchi, Y. Kubota and H. Kitagawa, *Journal of the American Chemical Society*, 2022, **144**, 3365-3369.

98. N. Kar, M. McCoy, J. Wolfe, S. L. A. Bueno, I. H. Shafei and S. E. Skrabalak, *Nature Synthesis*, 2024, **3**, 175-184.
99. Y. Chen, X. Zhan, S. L. A. Bueno, I. H. Shafei, H. M. Ashberry, K. Chatterjee, L. Xu, Y. Tang and S. E. Skrabalak, *Nanoscale Horizons*, 2021, **6**, 231-237.
100. S. L. A. Bueno, A. Leonardi, N. Kar, K. Chatterjee, X. Zhan, C. Chen, Z. Wang, M. Engel, V. Fung and S. E. Skrabalak, *ACS Nano*, 2022, **16**, 18873-18885.
101. S. Wang, W. Huo, F. Fang, Z. Xie, J. K. Shang and J. Jiang, *Chemical Engineering Journal*, 2022, **429**, 132410.
102. Y. Yao, Z. Li, Y. Dou, T. Jiang, J. Zou, S. Y. Lim, P. Norby, E. Stamate, J. O. Jensen and W. Zhang, *Dalton Transactions*, 2023, **52**, 4142-4151.
103. X. Lao, X. Liao, C. Chen, J. Wang, L. Yang, Z. Li, J.-W. Ma, A. Fu, H. Gao and P. Guo, *Angewandte Chemie International Edition*, 2023, **62**, e202304510.
104. H. Jiang, X. Liu, M.-N. Zhu, J. Xu, L. An, P.-F. Sui, J.-L. Luo and G. J. Cheng, *Science Advances*, 2022, **8**, eabm6541.
105. Y.-H. Liu, C.-J. Hsieh, L.-C. Hsu, K.-H. Lin, Y.-C. Hsiao, C.-C. Chi, J.-T. Lin, C.-W. Chang, S.-C. Lin, C.-Y. Wu, J.-Q. Gao, C.-W. Pao, Y.-M. Chang, M.-Y. Lu, S. Zhou and T.-H. Yang, *Science Advances*, 2023, **9**, eadf9931.
106. X. Zuo, R. Yan, L. Zhao, Y. Long, L. Shi, Q. Cheng, D. Liu and C. Hu, *Journal of Materials Chemistry A*, 2022, **10**, 14857-14865.
107. C. Zhan, L. Bu, H. Sun, X. Huang, Z. Zhu, T. Yang, H. Ma, L. Li, Y. Wang, H. Geng, W. Wang, H. Zhu, C.-W. Pao, Q. Shao, Z. Yang, W. Liu, Z. Xie and X. Huang, *Angewandte Chemie International Edition*, 2023, **62**, e202213783.
108. H. Minamihara, K. Kusada, D. Wu, T. Yamamoto, T. Toriyama, S. Matsumura, L. S. R. Kumara, K. Ohara, O. Sakata, S. Kawaguchi, Y. Kubota and H. Kitagawa, *Journal of the American Chemical Society*, 2022, **144**, 11525-11529.
109. K. Kusada, T. Yamamoto, T. Toriyama, S. Matsumura, K. Sato, K. Nagaoka, K. Terada, Y. Ikeda, Y. Hirai and H. Kitagawa, *The Journal of Physical Chemistry C*, 2021, **125**, 458-463.
110. M. Cui, C. Yang, S. Hwang, M. Yang, S. Overa, Q. Dong, Y. Yao, A. H. Brozena, D. A. Cullen, M. Chi, T. F. Blum, D. Morris, Z. Finfrock, X. Wang, P. Zhang, V. G. Goncharov, X. Guo, J. Luo, Y. Mo, F. Jiao and L. Hu, *Science Advances*, 2022, **8**, eabm4322.

111. Y. Nakaya, E. Hayashida, H. Asakura, S. Takakusagi, S. Yasumura, K.-i. Shimizu and S. Furukawa, *Journal of the American Chemical Society*, 2022, **144**, 15944-15953.
112. J. Ma, F. Xing, Y. Nakaya, K.-i. Shimizu and S. Furukawa, *Angewandte Chemie International Edition*, 2022, **61**, e202200889.
113. F. Xing, J. Ma, K.-i. Shimizu and S. Furukawa, *Nature Communications*, 2022, **13**, 5065.
114. W. Chen, S. Luo, M. Sun, X. Wu, Y. Zhou, Y. Liao, M. Tang, X. Fan, B. Huang and Z. Quan, *Advanced Materials*, 2022, **34**, 2206276.

Figures and Figure Captions

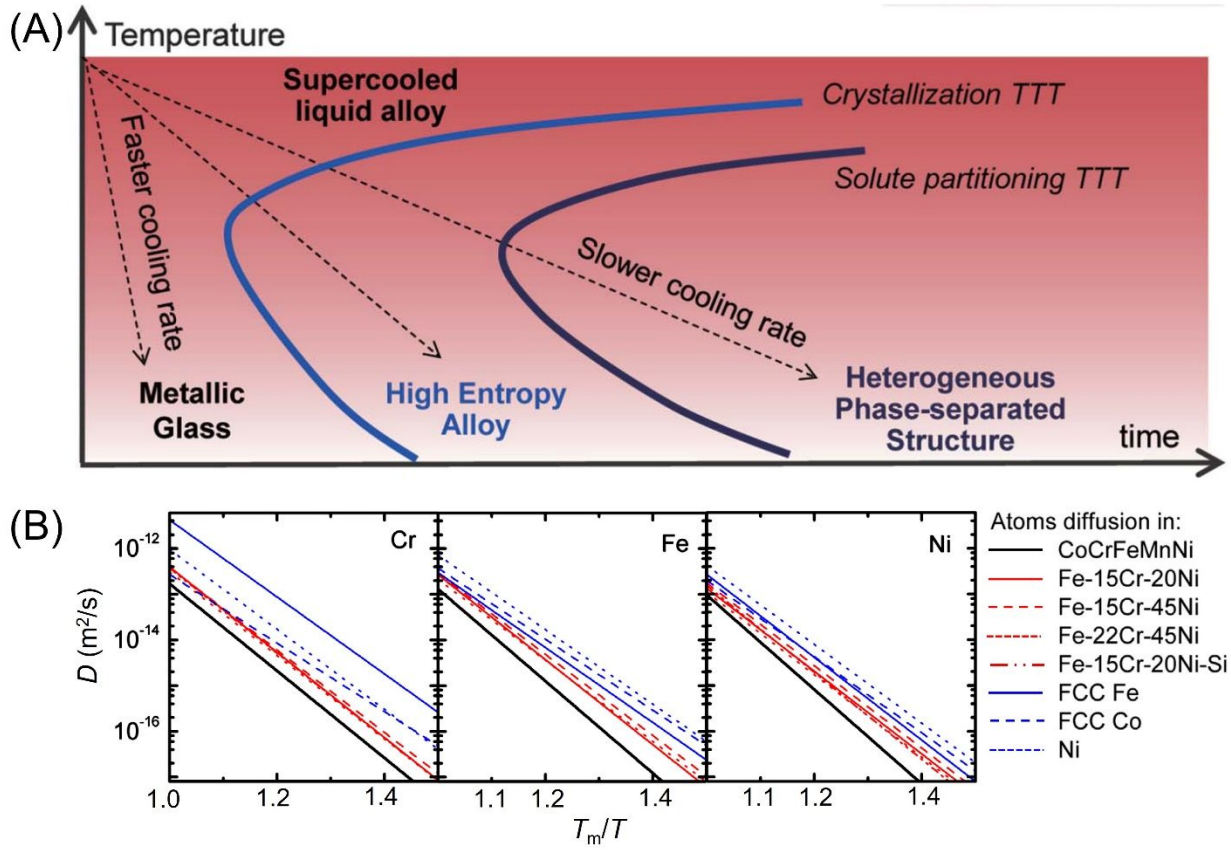

Figure 1 (A) Time-temperature transformation (TTT) diagram displaying the kinetic formation of amorphous metallic glass, single-phase high-entropy alloy (HEA), and phase-segregated structures, respectively, from a liquid alloy as a function of cooling rate. Adapted from ref. 4 with permission from The American Association for the Advancement of Science, copyright 2018. (B) Diffusion coefficients of Cr, Fe, and Ni as a function of temperature in different matrices, including single-element metals, simple alloys, and CoCrFeMnNi HEA. T_m is the solidus temperature for alloys. Adapted from ref. 5 with permission from Elsevier, copyright 2013.

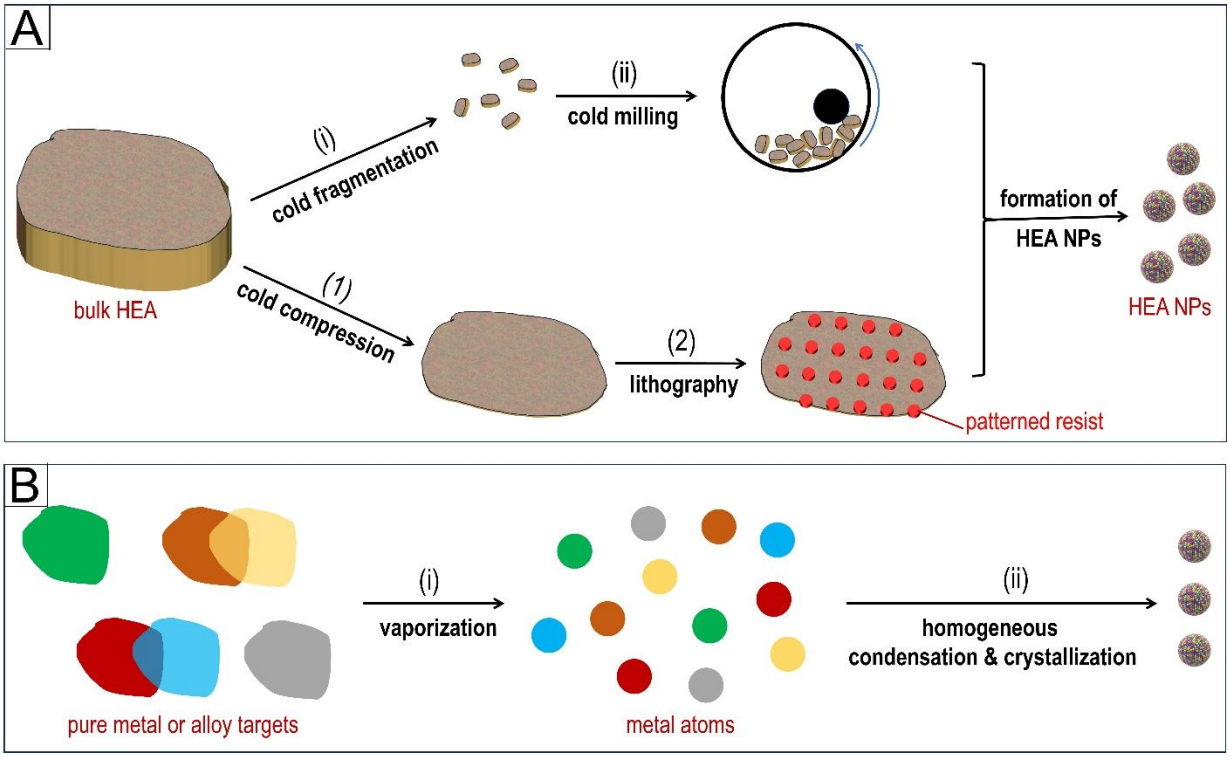

Figure 2 Synthesis of HEA nanoparticles from bulk metal targets. (A) "Physical Minimization of HEA Metals" through cold milling (top) and lithography (bottom). (B) Simultaneous "Vaporization of Metals" of different elements followed by simultaneous condensation and crystallization of metal atoms into HEA nanoparticles. HEA NPs = high-entropy alloy nanoparticles.

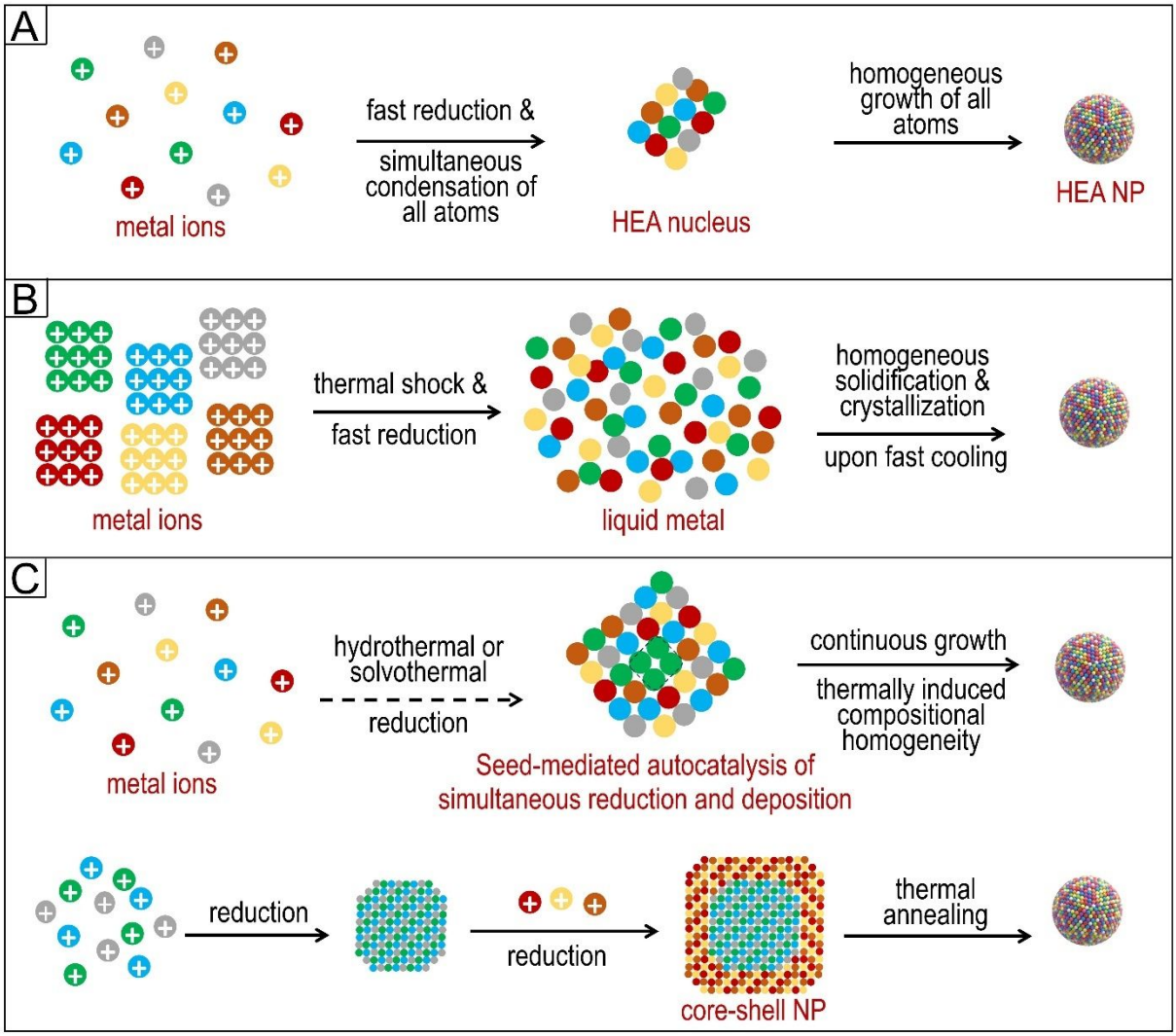

Figure 3 Bottom-up synthesis of HEA nanoparticles from metal precursor ions. (A) "Burst Reduction" of metal ions of different elements simultaneously followed by simultaneous precipitation of all metal atoms in both nucleation and growth steps. (B) "Thermal Shock" generating extremely high temperatures to simultaneously reduce all metal ions and melt the reduced metals within a very short period, followed by a fast temperature quenching to solidify the liquid metals into a solid-solution HEA nanocrystals. (C) "Solvothermal Reduction" of metal ions of different elements in a simultaneous manner (top) or a sequential manner (bottom), followed by annealing in the reaction solution or in an inert/reducing atmosphere for an extended period.

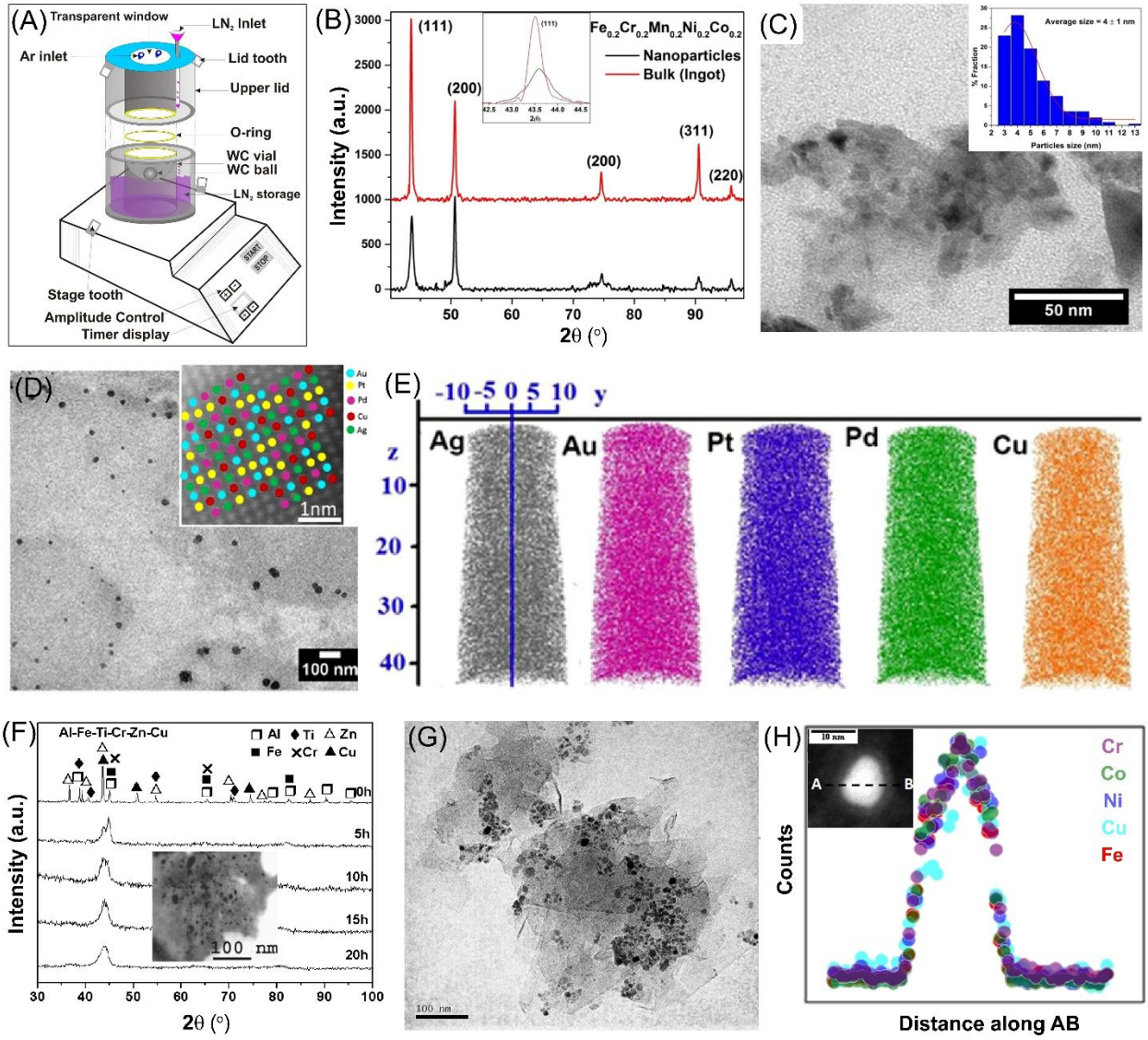

Figure 4 Synthesis of HEA nanoparticles via milling of bulk metals. (A) Schematic illustration of a single ball cryo-mill with a tungsten carbide (WC) vial and ball. (B) Comparison of XRD patterns of the FeCrMnNiCo HEA ingot and the cryo-milled HEA nanoparticles. (C) TEM image and particle size statistic histogram (inset) of the FeCrMnNiCo HEA nanoparticles. Adapted from ref. 31 with permission from Springer Nature, copyright 2018. (D) TEM bright-field image of AuAgPtPdCu HEA nanoparticles synthesized from cryo-milling of the corresponding HEA ingot. The inset is the high-resolution STEM image of one nanoparticle showing the lattice with different relative intensities marked with varying colors correlating to different elements. (E) Atomic probe tomography (APT) of the five elements showing the chemical homogeneity in the AuAgPtPdCu HEA nanoparticles. Adapted from ref. 33 with permission from American Chemical Society,

copyright 2020. (F) Evolution of XRD patterns in synthesizing AlFeTiCrZnCu HEA nanoparticles by milling pure metal powders at room temperature. The inset shows the TEM image of the synthesized HEA nanoparticles. Adapted from ref. 36 with permission from Elsevier, copyright 2008. (G) TEM image of NiFeCrCoCu HEA nanoparticles dispersed on graphene nanosheets synthesized by milling the mixture of graphite and pure metal powders at room temperature. (H) EDS line scan profiles of different elements across a HEA nanoparticle (inset). Adapted from ref. 38 with permission from Springer Nature, copyright 2018.

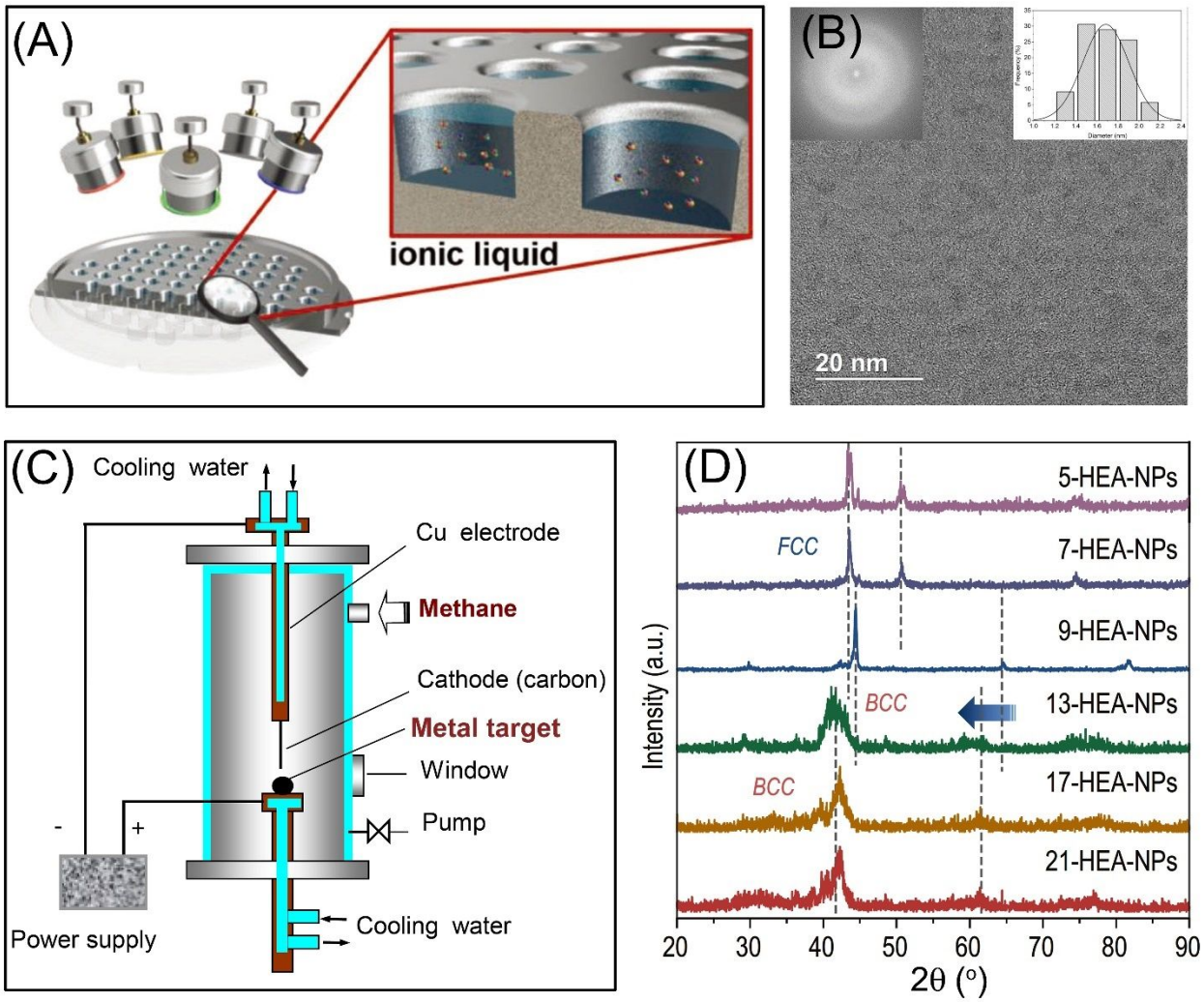

Figure 5 (A) Schematic illustration of the setup for synthesizing HEA nanoparticles by combinatorial co-sputtering pure metal targets into an ionic liquid. (B) TEM image, fast Fourier transform (FFT) (top left inset), and size distribution histogram (top right inset) of CrMnFeCoNi HEA nanoparticles synthesized from the DC co-sputtering. Adapted from ref. 40 with permission from John Wiley and Sons, copyright 2018. (C) Schematic illustration of the arc plasma chamber used for synthesizing HEA nanoparticles. Adapted from ref. 45 with permission from Springer Nature, copyright 2013. (D) XRD patterns of HEA nanoparticles with different element combinations up to 21 elements of FeCoNiCrYTiCuAlNbMoTaWZnCdPbBiAgInMnSn. Adapted from ref. 26 with permission from Oxford University Press, copyright 2022.

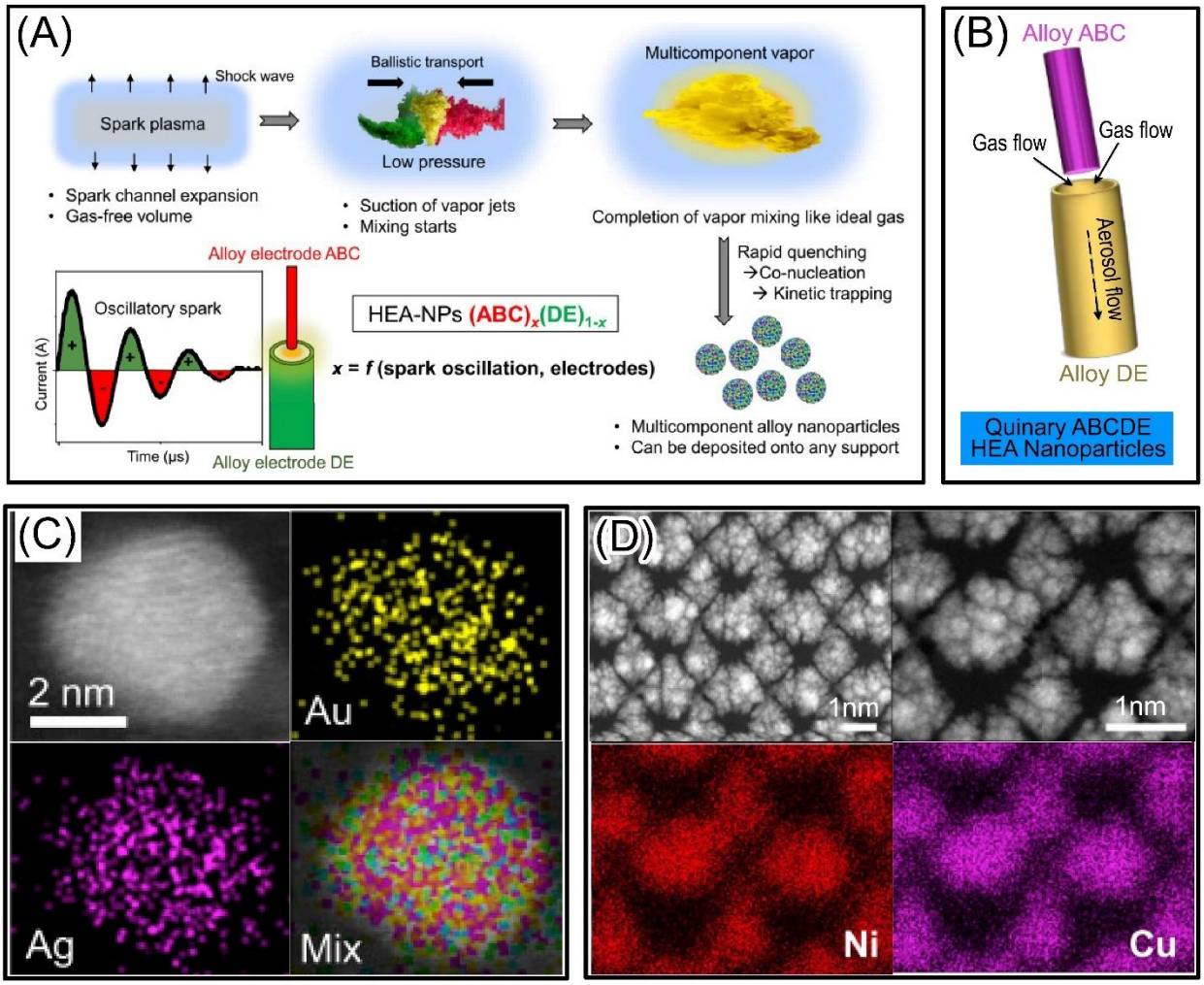

Figure 6 (A) Schematic illustration of the "sparking mashup" mechanism that vaporizes and mixes metal atoms in the spark plasma channel between two metal target electrodes. (B) Electrode configuration for synthesizing quinary HEA nanoparticles. (C) STEM image and EDS mapping of a senary AuNiAgCrCoMo HEA nanoparticle. (D) 3D-printed array of flower-like structures using the senary NiCrCoMoCuPd HEA nanoparticles collected downstream of the sparking mashup synthesis. The EDS mapping images of the rest elements are available in Ref. 48. Adapted from ref. 48 with permission from Elsevier, copyright 2020.

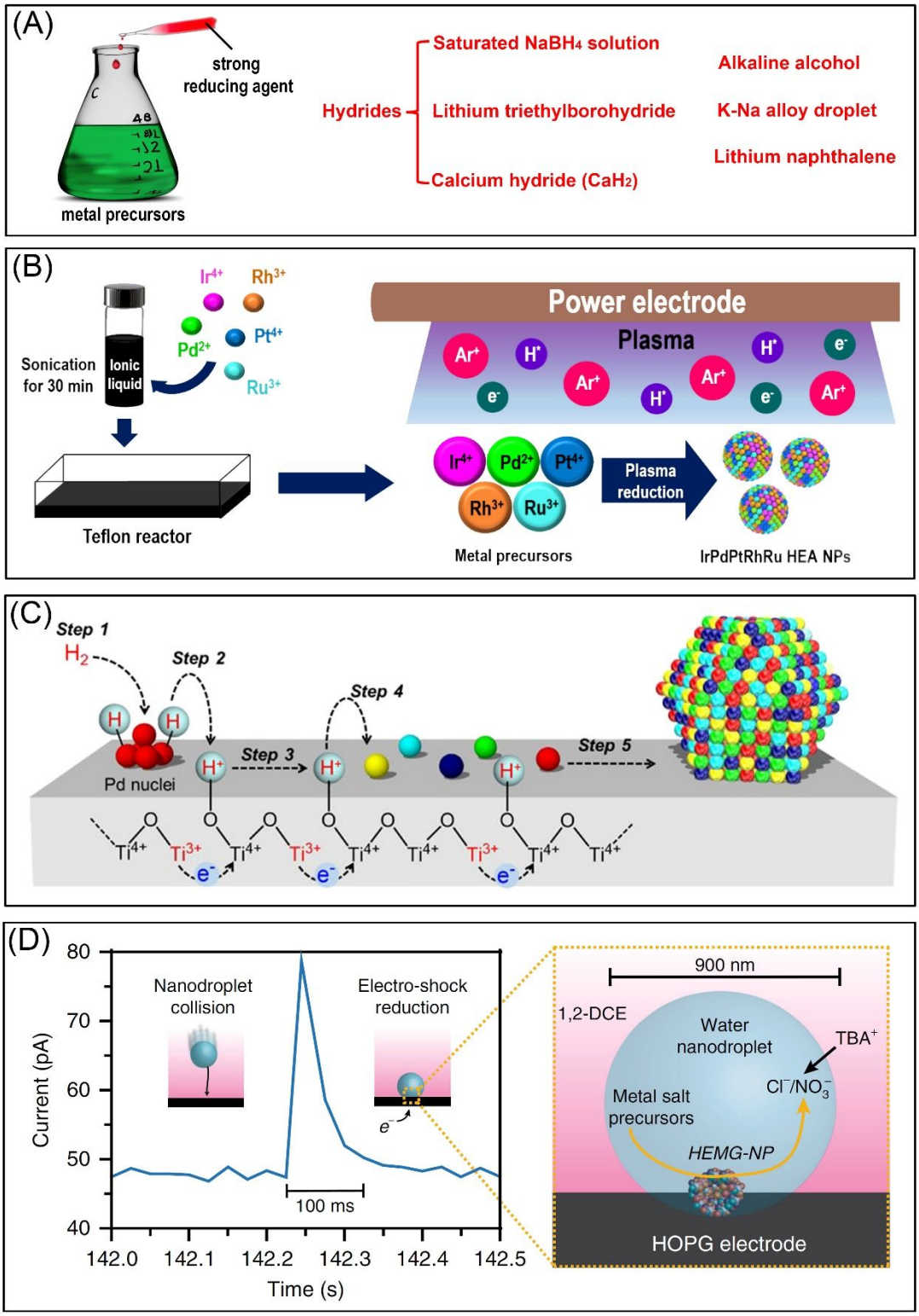

Figure 7 Burst reduction of metal precursor ions using species with very strong reducing power. (A) Reduction of metal ions using strong reducing agents. (B) Schematic illustration of the

synthesis of IrPdPtRhRu HEA nanoparticles using the wet plasma reduction of metal precursor ions in an ionic liquid. Adapted from ref. 66 with permission from Elsevier, copyright 2022. (C) Illustration of the mechanism responsible for synthesizing HEA nanoparticles on TiO_2 surface through hydrogen spillover reduction of metal ions. Adapted from ref. 69 with permission from Springer Nature, copyright 2021. (D) Electrochemical shock process for synthesizing HEA nanoparticles in nanodroplets. Left frame: typical transient current profile upon the collision of a single nanodroplet onto a carbon fiber UME biased at a negative potential that can simultaneously reduce metal precursor ions of different elements. The metal ions in the nanodroplet are fully (>98%) reduced within 100 ms. Right frame: representation of a nanodroplet collision event showing the rapid formation of HEA nanoparticles at the water/substrate interface and the charge balance in the aqueous solution ensured by the transfer of TBA^+ across the oil/water interface. Adapted from ref. 70 with permission from Springer Nature, copyright 2019.

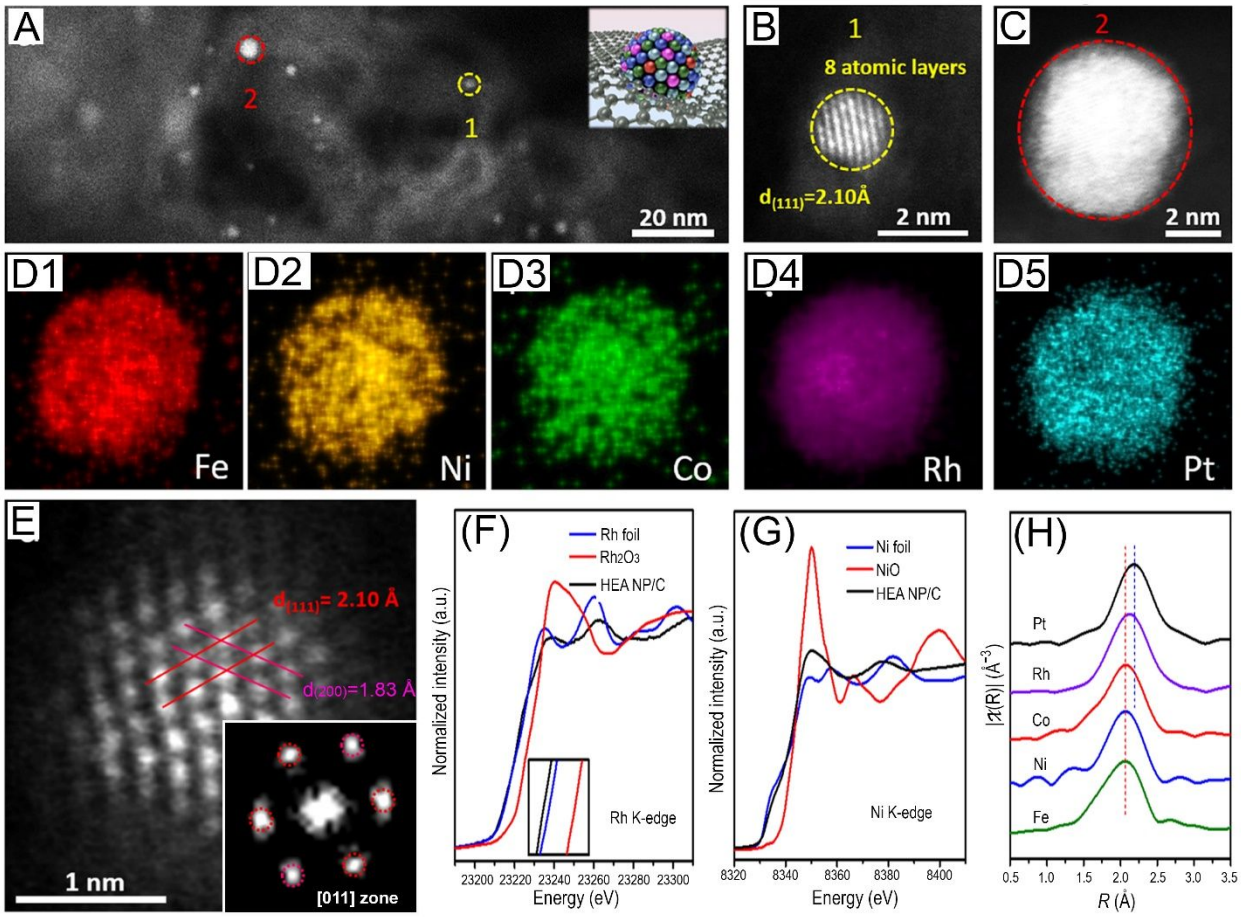

Figure 8 Characterization of the ultrasmall NiCoFePtRh HEA nanoparticles synthesized through burst reduction of metal ions with saturated $NaBH_4$. (A) HAADF-STEM image and model (inset) of the HEA nanoparticles on the carbon support. (B) Image of the smaller nanoparticles marked in (A) showing the lattice fringes with eight atomic layers. (C) Image of the larger nanoparticles marked in (A) and (D) the corresponding EDS mapping of different elements. (E) Atomically resolved HAADF-STEM image of one HEA nanoparticle clearly showing the {111} and {200} interplanar distances. The inset represents the FFT pattern that is consistent with the simulated diffraction pattern from the [011] zone axis of an fcc lattice, indicating that the image is taken by aligning the electron beam along the [011] direction of the nanoparticle lattice. (F) XANES spectra for the Rh K-edge. (G) XANES spectra for the Ni K-edge. (H) Extended XAFS spectra of all five elements for the NiCoFePtRh HEA nanoparticles. The offsets are added to enhance the visual clarity. Adapted from ref. 60 with permission from American Chemical Society, copyright 2021.

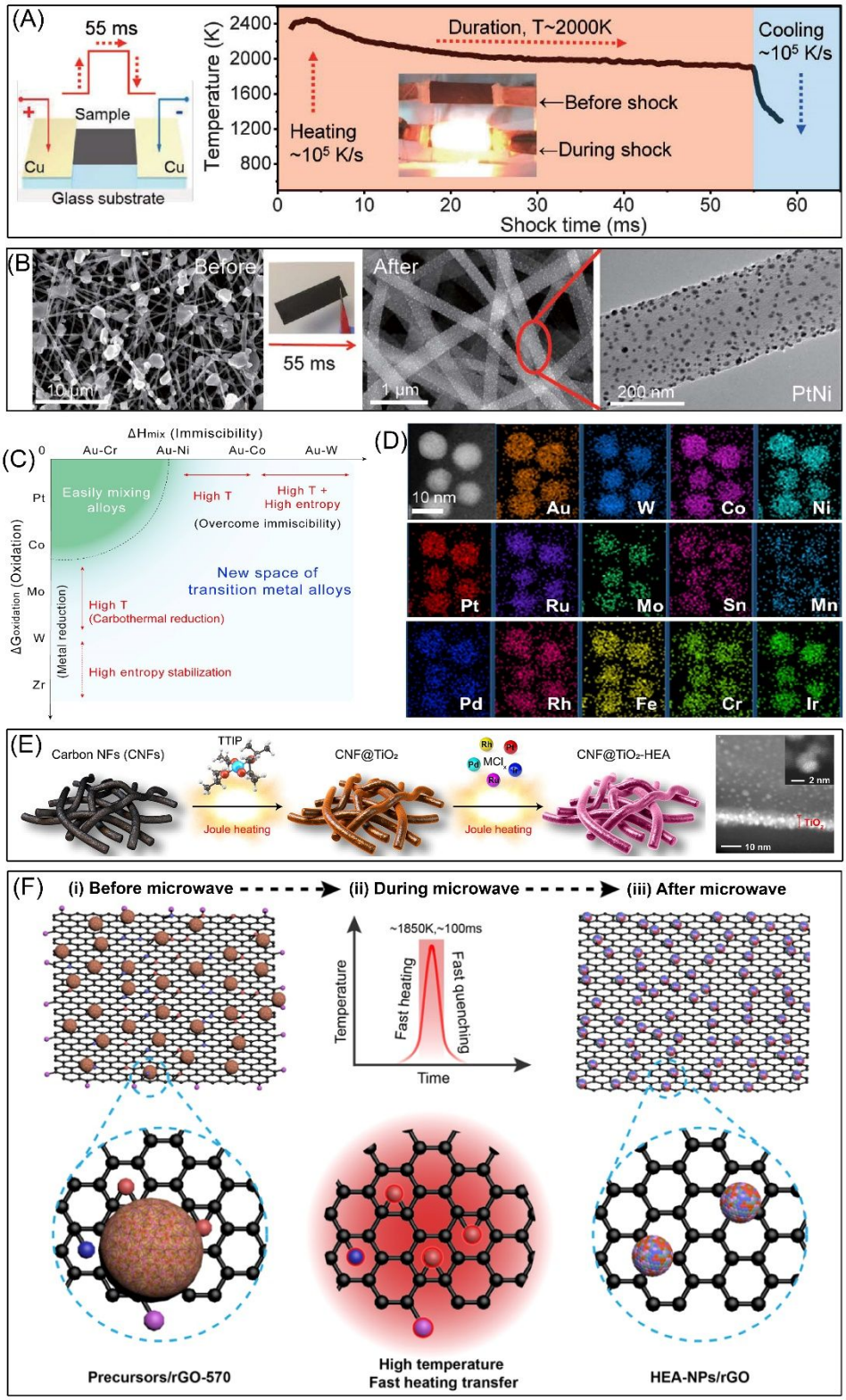

Figure 9 Carbothermal shock synthesis of HEA nanoparticles. (A) Schematic illustration of synthesizing HEA nanoparticles using the Joule-heating-induced carbothermal shock and the

temporal evolution of temperature during and after the short-period thermal shock. (B) Electron microscopy images of the metal precursor salt particles with micrometer sizes and broad size distributions on the carbon nanofiber support before thermal shock and the synthesized PtNi alloy nanoparticles well-dispersed on the carbon nanofibers after thermal shock. Adapted from ref. 4 with permission from The American Association for the Advancement of Science, copyright 2018. (C) Alloy space of transition metals at the nanoscale maximized by overcoming immiscibility and induced metal reduction through thermal shock induced high temperature and high entropy. The solid arrow indicates alloy formation in the range, while the dashed arrow indicates partial metal reduction and stabilization. (D) STEM image of 15-element AuWCuCoNiPtRuMoPdRhFeCrIrSnMn HEA nanoparticles and the corresponding EDS mapping of each element except Cu. The Cu grid generates a strong background signal of Cu. Adapted from ref. 76 with permission from Elsevier, copyright 2021. (E) Schematic illustration of the synthesis protocol for synthesizing HEA nanoparticles partially embedded in the TiO_2 layer coated on carbon nanofibers. The inset shows STEM images of the synthesized RuRhPdIrPt HEA nanoparticles, highlighting the spatial distribution of the HEA nanoparticles in reference to the TiO_2 layer. Adapted from ref. 78 with permission from American Chemical Society, copyright 2023. (F) Schematic illustration of synthesizing HEA nanoparticles on reduced graphene oxide (rGO) through microwave heating. Adapted from ref. 79 with permission from American Chemical Society, copyright 2021.

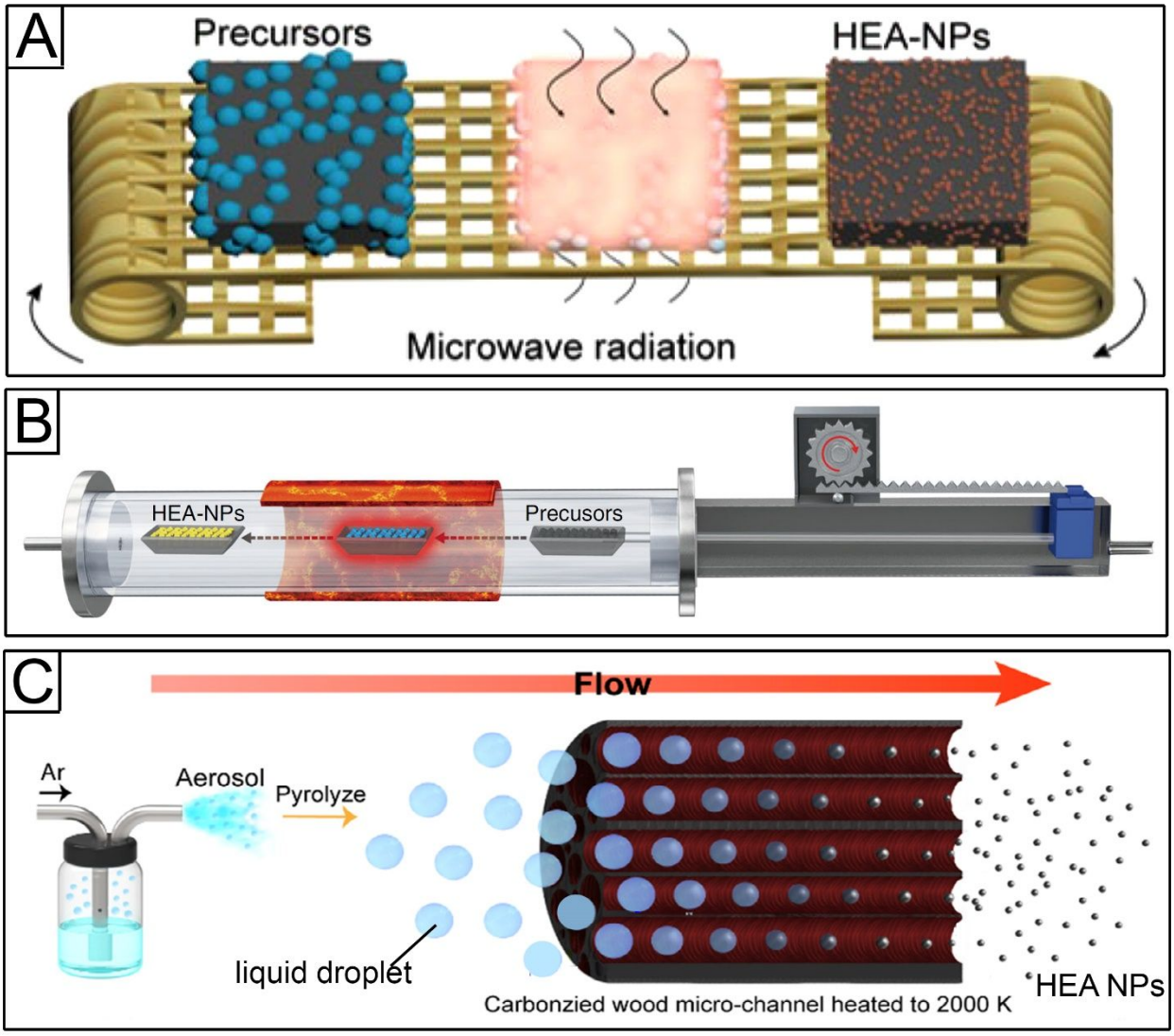

Figure 10 Continuous synthesis of HEA nanoparticles using various thermal shock methods. (A) Roll-to-roll process using the microwave heating method. Adapted from ref. 79 with permission from American Chemical Society, copyright 2021. (B) Fast-moving bed pyrolysis (FMBP) setup showing the transport of metal precursor powder to the heating zone. Adapted from ref. 80 with permission from Springer Nature, copyright 2020. (C) Schematic drawing of the aerosol microdroplets transporting through the carbonized wood micro-channels heated to 2000 ^{o}C using the carrier gas. Adapted from ref. 82 with permission from Elsevier, copyright 2020.

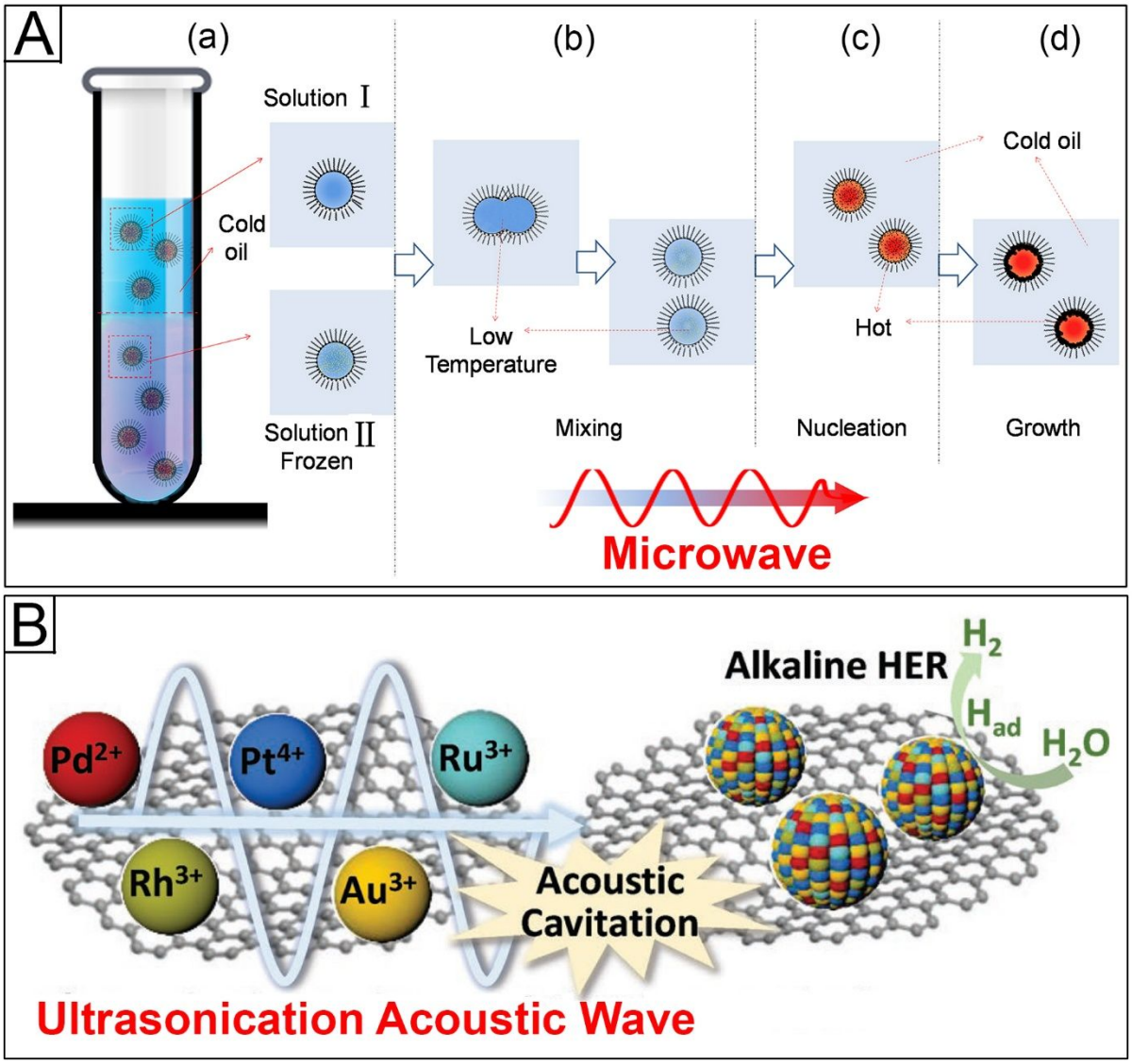

Figure 11 (A) Schematic illustration of the major steps involved in synthesizing colloidal metal alloy nanoparticles of immiscible element combinations through microwave-assisted flash heating and cooling in micelle nanoreactors. Adapted from ref. 83 with permission from John Wiley and Sons, copyright 2018. (B) Schematic illustration of synthesizing carbon-supported PtAuPdRhRu HEA nanoparticles using ultrasonication. Adapted from ref. 85 with permission from John Wiley and Sons, copyright 2019.

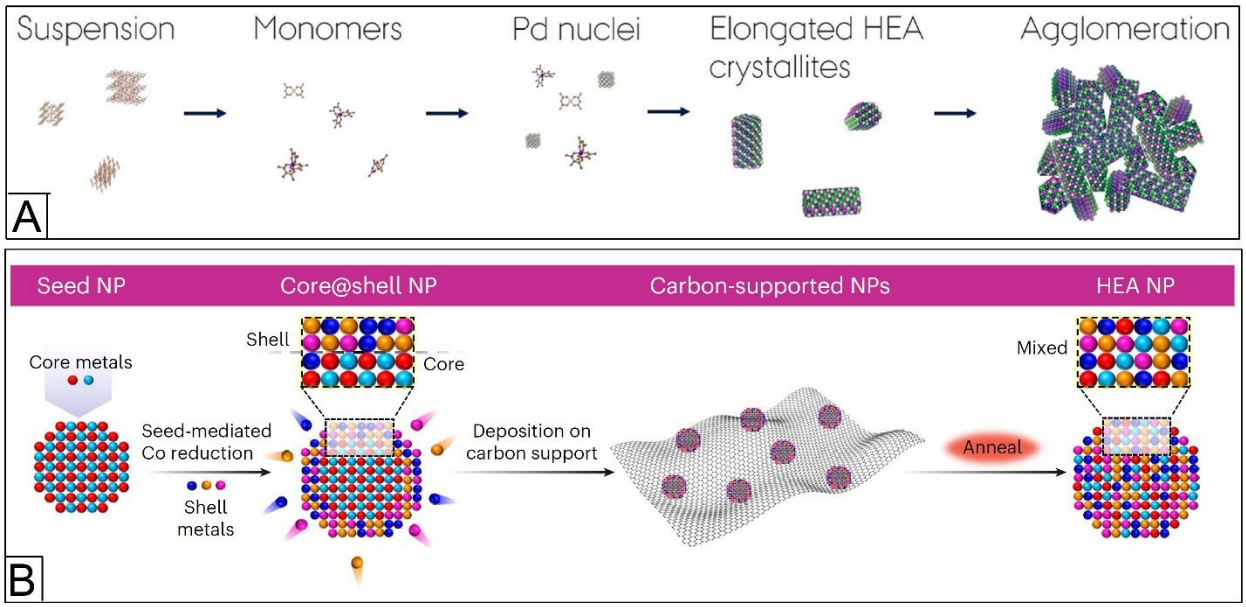

Figure 12 (A) Schematic description of the formation mechanism for PtIrPdRhRu HEA nanoparticles under solvothermal conditions, highlighting that the initially formed Pd-rich nuclei drive autocatalysis for simultaneous reduction of metal precursor ions of different elements and simultaneous precipitation of the reduced metal atoms. Adapted from ref. 88 with permission from John Wiley and Sons, copyright 2020. (B) Schematic illustration of synthesizing core-shell nanoparticles made of multi-principal elements and their conversion into HEA nanoparticles upon thermal annealing. Adapted from ref. 98 with permission from Springer Nature, copyright 2023.

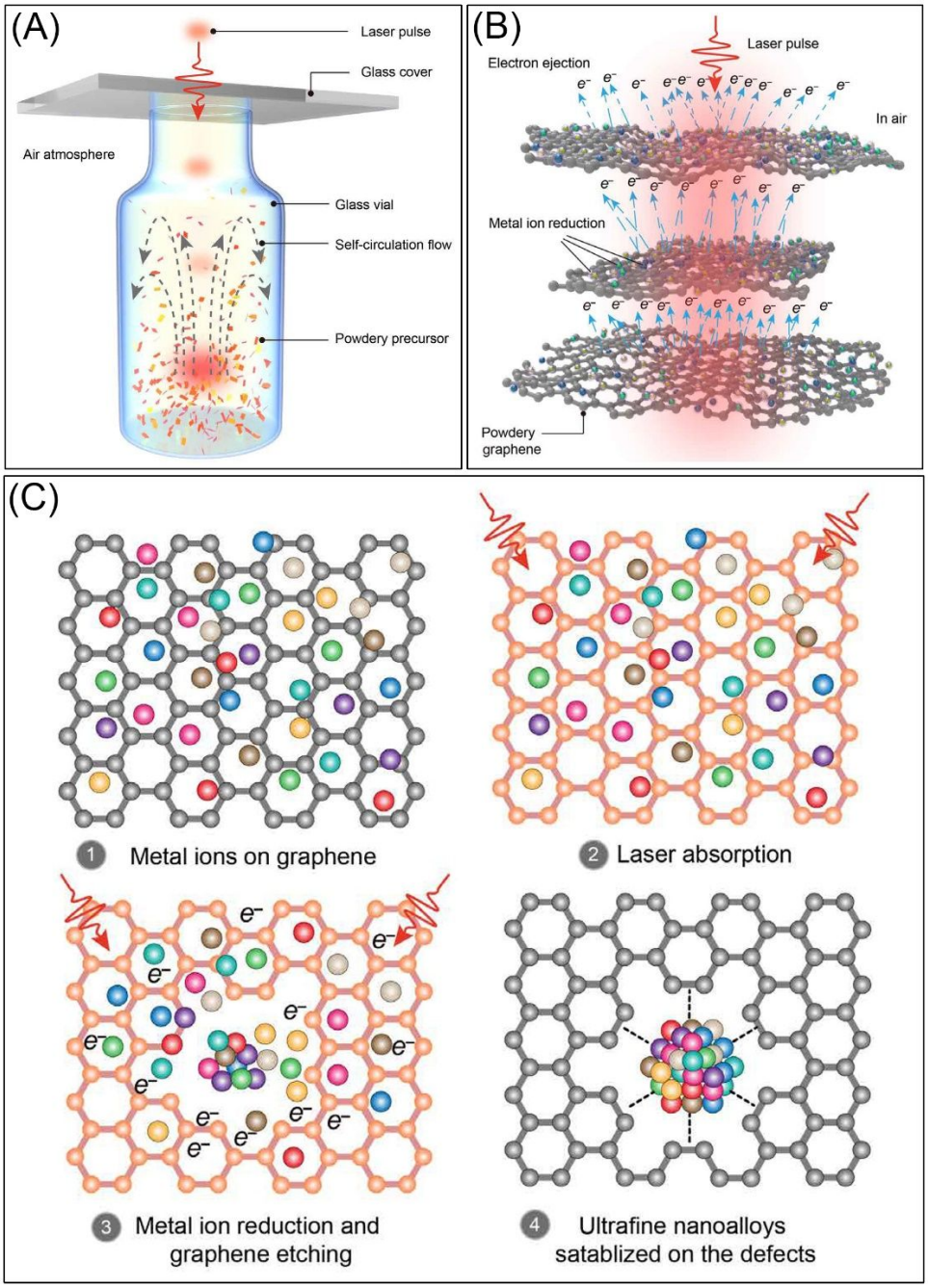

Figure 13 Schematic illustration of the laser-induced thermionic emission reduction mechanism for synthesizing HEA nanoparticles on carbon support. (A) Laser propulsion of graphene sheets in a glass vial enabling uniform irradiation and reduction of the metal precursor salts loaded on graphene. (B) Laser-induced electron emission from graphene reducing metal ions loaded on graphene surface. (C) Four steps for the formation of HEA nanoparticles stabilized on graphene at

the defect sites. Adapted from ref. 104 with permission from The American Association for the Advancement of Science, copyright 2022.